Revision 1

Some thermodynamic properties of larnite (β-Ca_2SiO_4) constrained by high *T*/*P* experiment and/or theoretical simulation

ZHIHUA XIONG,[1,2] XI LIU,[1,2,*] SEAN R. SHIEH,[3] SICHENG WANG,[1,2] LINLIN CHANG,[4] JUNJIE TANG,[1,2] XINGUO HONG,[5] ZHIGANG ZHANG,[6] AND HEJING WANG[1,2]

[1] The Key Laboratory of Orogenic Belts and Crustal Evolution, Ministry of Education of China, Beijing 100871, China

[2] School of Earth and Space Sciences, Peking University, Beijing 100871, China

[3] Department of Earth Sciences, University of Western Ontario, London, Ontario, N6A 5B7, Canada

[4] College of Earth Science, University of Chinese Academy of Sciences, Beijing 100049, China

[5] Mineral Physics Institute, State University of New York, Stony Brook, New York 11974, USA

[6] Key Laboratory of Earth and Planetary Physics, Institute of Geology and Geophysics, Chinese Academy of Sciences, Beijing 100029, China

*Corresponding Author: Xi Liu

Email: xi.liu@pku.edu.cn Tel: 86-10-6275-3585 Fax: 86-10-6275-2996

24

25 Running Title: THERMODYNAMIC PROPERTIES OF LARNITE

26

ABSTRACT

Pure larnite (β-Ca_2SiO_4; Lrn) was synthesized at 6 GPa and 1473 K for 6 hours by using a cubic press, its thermal expansivity was investigated up to 923 K by using an X-ray powder diffraction technique (ambient P), and its compressibility was investigated up to ~16 GPa by using a diamond-anvil cell coupled with synchrotron X-ray radiation (ambient T). Its volumetric thermal expansion coefficient (α_V) and isothermal bulk modulus (K_T) were constrained as $\alpha_V = 4.24(4)\times10^{-5}$/K and $K_T = 103(2)$ GPa (the first pressure derivative K_T' obtained as 5.4(4)), respectively. Its compressibility was further studied with the CASTEP code using density functional theory and planewave pseudopotential technique. We obtained the K_T values as 123(3) GPa (LDA; high boundary) and 92(2) GPa (GGA; low boundary), with the values of the K_T' as 4.4(9) and 4.9(5), respectively. The phonon dispersions and vibrational density of states (VDoS) of Lrn were simulated using density functional perturbation theory, and the VDoS was combined with a quasi-harmonic approximation to compute the isobaric heat capacity (C_P) and standard vibrational entropy (S_{298}^0), yielding $C_P = 212.1(1) - 9.69(5)\times10^2T^{-0.5} - 4.1(3)\times10^6T^{-2} + 5.20(7)\times10^8T^{-3}$ J mol^{-1} K^{-1} for the T range of ~298-1000 K and S_{298}^0 = 129.8(13) J mol^{-1} K^{-1}. The microscopic and macroscopic thermal Grüneisen parameters of Lrn at 298 K were calculated to be 0.75(6) and 1.80(4), respectively.

Keywords: β-Ca_2SiO_4, compressibility, entropy, heat capacity, larnite, thermal expansivity, thermal Grüneisen parameter, thermodynamic property

INTRODUCTION

Natural larnite (Lrn; β-Ca_2SiO_4; space group $P2_1/n$ with Z = 4) was firstly reported in the Larne district of Great Britain (Tilley 1929), and soon documented on the island of Muck in Scotland (Tilley 1947) and the Tokatoka region in New Zealand (Mason 1957). It usually locates in the contact zone between an igneous rock like dolerite or andesite, and a calcitic rock such as chalk or limestone (Tilley 1929; Mason 1957). Lrn commonly coexists with spurrite, melilite, merwinite and spinel, and readily transforms to the olivine-structured Ca_2SiO_4 phase (the γ-Ca_2SiO_4 phase) if it is shocked or heated at certain temperature (Tilley 1929). According to Bowen (1940) and Tilley (1951), Lrn generally represents the high-T stage of the progressive metamorphism (or decarbonation) of the siliceous limestones.

This conventional field occurrence of Lrn was recently supplemented with another completely different appearance, tiny mineral inclusions, usually coexisting with the walstromite-structured $CaSiO_3$ (Wal) and titanite-structured $CaSi_2O_5$ (Ttn), in diamonds possibly originating from the lower mantle (Joswig et al. 1999; Nasdala et al. 2003; Brenker et al. 2005). This new appearance argues that some portions of the deep interior of the Earth are significantly Ca-richer than the normal pyrolitic mantle (Ringwood 1975). According to the results from some high-P experimental studies (e.g., Green and Ringwood 1967; Takahashi 1986; Irifune 1994), the Ca-rich silicate in the normal mantle normally changes from clinopyroxene, majoritic garnet to calcium perovskite (CaPv; compositionally close to $CaSiO_3$) as P increases from the surface to the

core-mantle boundary of the Earth. In order to stabilize Lrn, Wal and Ttn, significantly higher levels of CaO should be introduced into the mantle, which has been presumably accomplished via deep subduction of the CaO-rich continental crust material (Irifune et al. 1994; Liu et al. 2012a).

It is well known that Lrn is not a stable phase at ambient P (Fig. 1a). From low T to high T, the composition of Ca_2SiO_4 can form many polymorphs, namely γ-Ca_2SiO_4, α'_L-Ca_2SiO_4, α'_H-Ca_2SiO_4 and α-Ca_2SiO_4 (e.g., Barnes et al. 1980; Remy et al. 1995, 1997a, 1997b; Yamnova et al. 2011). Lrn never forms during heating, but appears as a metastable phase in the stability field of the γ-Ca_2SiO_4 phase during cooling. Consequently, it was usually synthesized by heating the Ca_2SiO_4 composition in the stability field of the phase α'_L-Ca_2SiO_4, α'_H-Ca_2SiO_4 or α-Ca_2SiO_4, and then quickly quenching into water (Remy et al. 1997a, 1997b; Fukuda et al. 1997), a process which might introduce different amounts of defects in the products (e.g., twins are common in Lrn; Groves 1983; Kim et al. 1992). In order to preserve the Lrn structure, some "stabilizer" such as P_2O_5 (Saalfeld 1975), B_2O_3 (Remy et al. 1997a), vacancy of either Ca (Rodrigues 2003) or Si (Yannaquis and Guinier 1959), or other species (Lai et al. 1992) was usually introduced into the system.

According to the phase diagram of the composition Ca_2SiO_4 at high-P and high-T conditions (Fig. 1b), Lrn has a vast stability field. At the low P side, Lrn transforms to the γ-Ca_2SiO_4 phase at ~2 GPa and room T (Hanic et al. 1987; Remy et al. 1995, 1997b; Reynard et al. 1997), and the invariant point of β-Ca_2SiO_4 + γ-Ca_2SiO_4 + α'_L-Ca_2SiO_4 locates at ~0.34 GPa and 711 K (Hanic et al. 1987). At the high P side, the relationship

between Lrn and the α'_L-Ca_2SiO_4 phase (Wang and Weidner 1994) or K_2NiF_4-structured Ca_2SiO_4 phase (Liu 1978) is still poorly constrained (Fig. 1b).

Lrn also participates in some other geologically important reactions such as

$$3Wal = Ttn + Lrn \quad (1)$$

and

$$Ttn + Lrn = 3CaPv \quad (2),$$

with the former taking place at ~8 GPa and the latter at ~12 GPa (Kanzaki et al. 1991; Wang and Weidner 1994; Akaogi et al. 2004; Sueda et al. 2006). To understand these reactions, especially the one related to the CaPv, which is the dominant Ca-bearing phase in the lower mantle of the Earth (Mao et al. 1977; Irifune et al. 1989) but unfortunately unquenchable to room *P* for further characterizations such as single crystal crystallographic study and calorimetric investigation (Liu and Ringwood 1975; Mao et al. 1977; Irifune 1994), it is necessary to investigate the thermodynamic properties of Lrn as extensively and accurately as possibly. These thermodynamic properties of Lrn then can be combined with the thermodynamic properties of Ttn to rigorously constrain the thermodynamic properties of CaPv via an accurate experimental determination of the *P*-*T* conditions of equation (2). The thermal expansivity of Lrn has been investigated by different techniques, but the volumetric thermal expansion coefficient at 298 K (α_{298}) varies from ~1.80×10^{-5} to 4.25×10^{-5} K^{-1} (e.g., Remy et al. 1997b; Swamy and Dubrovinsky 1997). The isothermal bulk modulus (K_T) of Lrn has also been investigated (Remy et al. 1997b; Swamy and Dubrovinsky 1997), but its value at 298 K varies from ~119 to 166(15) GPa (the first pressure derivative of K_T, K_T', set as 4). Heat capacity measurements have been performed from 52.66 to 296.48 K (Todd 1951) and from 406.0

to 964.6 K (Coughlin and O'Brien 1957). With an empirical sum equation of Debye and Einstein functions to extrapolate the heat capacity data down to zero K, an S^0_{298} value as 127.6(8) J mol^{-1} K^{-1} has been derived, which has never been verified by any means so far. It thus appears that a substantial amount of work has to be conducted in order to fully understand the thermodynamic features of Lrn.

In this study, we synthesized pure Lrn in its *P*-*T* stability field by using a massive cubic press, and determined its thermal expansivity by using an in situ high-*T* powder X-ray diffraction method (ambient *P*), and its compressibility by using a synchrotron X-ray radiation combined with a diamond-anvil cell (DAC; ambient *T*). Its compressibility was further studied with the CASTEP code using density functional theory and planewave pseudopotential technique. Using density functional perturbation theory, its phonon dispersions and vibrational density of states (VDoS) were simulated, and the VDoS was combined with a quasi-harmonic approximation to compute the isobaric heat capacity (C_P) and vibrational entropy (S). Finally, the microscopic and macroscopic thermal Grüneisen parameters of Lrn at the ambient *P*-*T* condition were calculated.

EXPERIMENTAL AND SIMULATING METHODS

The polycrystalline Lrn sample used in our thermal expansion and compression experiments was synthesized with the CS-IV 6×14 MN cubic press at the High-Pressure Laboratory of Peking University (Liu et al. 2012b). In the high-*P* synthesizing experiments, we used the assembly BJC-1 (Liu et al. 2012c), with its pressure calibrated

at ambient *T* by using the high-*P* phase transitions of Bi (I-II transition at 2.55 GPa, and II-III transition at 2.69 GPa) and Ba (I-II transition at 5.5 GPa). The temperature in the high-*P* synthesizing experiments was measured and controlled by employing a $Pt_{94}Rh_6$-$Pt_{70}Rh_{30}$ thermocouple (type B), with any potential pressure effect on the e.m.f. ignored. We prepared the starting material for the high-*P* synthesizing experiments with the following steps: we firstly mixed under acetone the powders of SiO_2 and $CaCO_3$ in a molar ratio of 1:2, which were pretreated at 1 atm and 573 K for 72 hours; we secondly pressed this mixture into a pellet and degassed it at 1 atm and 1273 K for about 48 hours; we thirdly crushed finely the pellet under acetone into a powder, which was later stored at 383 K in a drying oven. The starting material for the high-*P* synthesizing experiments was sealed into an *h*BN capsule. The synthesizing conditions were 6 GPa and 1473 K with a heating time of 6 hours. In total we conducted five high-*P* synthesizing experiments under nominally identical physical conditions, and obtained four coherent samples and one dust-like sample. It appeared that some unknown factor played a role in the high-*P* synthesizing process.

Some portions of the coherent samples from the high-*P* synthesizing experiments were processed and examined by a scanning electron microscope (Quanta 650 FEG), a confocal micro-Raman system (Renishaw system RM-1000) and an electron microprobe (JEOL JXA-8100), and confirmed to be pure Lrn. Other portions of these samples were slowly ground down to a fine powder, which was used in our thermal expansion and compression experiments.

The thermal expansion experiments at ambient *P* were carried out with an X'Pert Pro MPD diffractometer system equipped with an Anton Paar HTK-1200N oven. A

Eurotherm temperature controller (Eurotherm 2604) collected with a type S thermocouple, which was checked against the melting point of NaCl, was used to control the temperature. Other details of the X'Pert Pro MPD diffractometer system included a Cu target, operation voltage of 40 kV and current of 40 mA. The whole experimental system was carefully checked up to 1273 K by using quartz as an internal standard (Hu et al. 2011). Following the heating and data-collection procedures reported in Liu et al. (2010), we carried out the high-*T* experiments up to 1023 K. At every studied *T*, X-ray data were collected from 10 to 70°2θ, with a scanning step length of 0.017°2θ and a scanning time of 10 seconds for each scanning step. As demonstrated by He et al. (2011) and Wang et al. (2012), unit-cell parameters with high accuracy were readily extracted by a full powder X-ray pattern refinement with the MDI's program Jade 6.0 (Material Data, Inc.).

The high-*P* angle dispersive X-ray diffraction experiments (ambient *T*) were conducted with a symmetrical DAC at the beamline X17C, National Synchrotron Light Source, Brookhaven National Laboratory. The experimental techniques were generally identical to those used in our previous studies (e.g., Liu et al. 2011; He et al. 2012; Xiong et al. 2015): a T301 stainless steel plate was used as the gasket, a 4:1 methanol-ethanol mixture as the pressure medium, and a couple of ruby chips used as the pressure marker (the ruby fluorescence method; Mao et al. 1978). The incident synchrotron radiation beam had a wavelength of 0.409929 Å, and its size was ~25 × 20 μm^2. Each X-ray diffraction pattern at certain *P* was collected for 60 minutes using an online CCD detector, and later processed to generate the conventional one-dimension profile using the Fit2D program (Hammersley 1996). Subsequently, the positions of the diffraction peaks were

186 determined with the Jandel Scientific PeakFit V4.11 program, and the unit-cell
187 parameters were obtained by using the UnitcellWin program.

188 The first-principles simulations carried out to investigate the compression
189 behavior of Lrn were completed with the CASTEP code using density functional theory
190 (Hohenberg and Kohn 1964; Kohn and Sham 1965) and planewave pseudopotential
191 technique (Payne et al. 1992). We treated the exchange-correlation interaction by both the
192 local density approximation (LDA) (Ceperley and Alder 1980; Perdew and Zunger 1981)
193 and generalized gradient approximation (GGA) with the Perdew-Burker-Ernzerhof
194 functional (Perdew et al. 1996), and used a convergence criterion of 10^{-6} eV/atom on the
195 total energy in the self-consistent field calculations. We employed a planewave basis set
196 with a cutoff of 900 eV to expand the electronic wave functions, and a norm-conserving
197 pseudopotential to model the ion-electron interaction (Lin et al. 1993; Lee 1995). We
198 sampled the irreducible Brillouin zone with a 4×3×2 Monkhorst-Pack grid (Monkhorst
199 and Pack 1976). The effects of using larger cutoff and k point mesh on the calculated
200 properties were found to be insignificant. The computation cell contained four Ca_2SiO_4
201 molecules (28 atoms), with the initial structure model from Tsurumi et al. (1994). The
202 equilibrium lattice parameters and internal coordinates at different pressures were
203 optimized by minimizing the Hellmann-Feynman force on the atoms and simultaneously
204 matching the stress on the unit cell to the target stress. These theoretical techniques were
205 used in our previous studies targeting the structures and thermodynamics of some silicate
206 minerals (e.g., Deng et al. 2010, 2011; Chang et al. 2013).

207 Based on the optimized structure with the LDA method, the phonon dispersions
208 and VDoS of Lrn were calculated by diagonalizing the dynamical matrix whose elements

209 were obtained using density functional perturbation theory (Baroni et al. 2001; Refson et
210 al. 2006). The q-vector grid spacing for interpolation was 0.05 $Å^{-1}$, which represented the
211 average distance between the Monkhorst-Pack q-points used in the dynamical matrix
212 calculations. The phonon dispersions were obtained at the high symmetry points (Z, G, Y,
213 A, B, D, E, C). The coordinates of these points on the surface of the Brillouin zone were
214 Z = (0 0 ½), G = (0 0 0), Y = (0 ½ 0), A = (-½ ½ 0), B = (-½ 0 0), D = (-½ 0 ½), E = (-½
215 ½ ½) and C = (0 ½ ½).
216
217
218 **RESULT AND DISCUSSION**
219
220 High-*P* synthesizing of pure Lrn
221 The BSE images taken from the polished surfaces of the coherent samples suggest
222 two coexisting phases: the predominant phase has a volume percentage higher than ~98%,
223 appears relatively dark, and attains a grain size of ~10-50 μm; the trace phase appears
224 relatively bright and has a grain size of ~1-2 μm. 10 electron microprobe analyses were
225 conducted on 10 arbitrarily selected grains of the predominant phase, and their average is
226 $Ca_{2.02(2)}Si_{0.99(1)}O_4$, suggesting a homogeneous composition closely matching the
227 stoichiometry of Lrn. 10 Raman spectra were collected on 10 arbitrarily selected grains of
228 the predominant phase, and they are similar, and in excellent agreement with the Raman
229 data of Lrn reported by Piriou and McMillan (1983) and Remy et al. (1997a). It follows
230 that the predominant phase in the coherent samples is Lrn indeed. On the other hand, the
231 trace phase is mostly likely a reaction residue (CaO) left from the formation of Lrn.

As suggested by our preliminary Raman spectroscopic data, the dust-like sample is distinctly dominated by the γ-Ca_2SiO_4 phase, which could be produced during temperature quenching or pressure release. The Ca_2SiO_4 system is infamous in its back-transformation (either partial or complete) of its high-*T* polymorphs at room *P* (Fig. 1a), and the operating factors include the maximum synthesizing *T*, the cooling kinetics, the grain size, and the release of strains and charge repulsions in the β-Ca_2SiO_4 phase (Remy et al. 1997a). Our observation made in this study similarly suggests that the back-transformation process is not always escapable for the samples synthesized at high *P*, in agreement with Remy et al. (1995) and Reynard et al. (1997). Anyhow, the first attempt in synthesizing a large amount of pure Lrn in its *P*-*T* stability field (Fig. 1b) has been at least partially successful, in spite of the complication caused by the back-transformation process.

It is worthy to point out that the univariant curve of $\beta = \alpha'_L$ determined by Klement and Cohen (1974) and Hanic et al. (1987) may be reasonably extrapolated to ~6 GPa (Fig. 1b). Assuming there was no any back-transformation from the α'_L phase to the Lrn phase in our synthetic samples, the *P*-*T* condition (6 GPa and 1473 K) of our synthesizing experiments does support this extrapolation. In contrast, the *P*-*T* condition (9 GPa and 1350 K) for the phase transition from the Lrn phase to the α'_L phase constrained by the in situ synchrotron X-ray experiments of Wang and Weidner (1994) does not. More high-*P* experimental investigation on this issue seems necessary.

High-*T* phase transition and thermal expansion coefficient (room *P*)

High-*T* X-ray diffraction experiments were conducted up to 1023 K at ambient pressure (Fig. 2). We found that all major X-ray diffraction peaks observed at temperatures below 973 K could be attributed to the Lrn phase (Jost et al. 1977; Yamnova et al. 2011), and the new peaks appearing from 973 K on could be attributed to the α'_L phase (ideally Ca_2SiO_4; Saalfeld 1975). As shown in Fig. 1(a), the stable form of Ca_2SiO_4 at relatively low *T* is the γ phase; its formation from the metastable Lrn phase was not observed in our experiments though. This phase transition is thus generally sluggish, in good agreement with the observation made by Remy et al. (1997a). The mechanism in this phase transition has been regarded as complicated and not fully understood, with the affecting factors presumably including the synthesizing condition, impurity and grain size of the used Lrn material, and the details of the heating process (Remy et al. 1997a; references therein).

The phase transition *T* from the metastable Lrn to the α'_L phase on heating was located between 923 and 973 K by our experiments (Fig. 2). In contrast, it was constrained between 960(5) to 988(5) K by in situ high-*T* Raman spectroscopy (Remy et al. 1997a) and between 984(10) to 1005(10) K by in situ high-*T* powder X-ray diffraction (Remy et al. 1997b). Taking into account the differences in the used materials and heating processes in these studies, the agreement is good.

The variation of the unit-cell parameters of the Lrn phase with *T* as determined in this study is shown in Fig. 3, and it is almost linear for the investigated *T* interval. This result is in general agreement with Fukuda et al. (1997), but contradicts Remy et al. (1997b): the data from Remy et al. (1997b) clearly demonstrated non-linear correlations between the *a*-axis and *T* (Fig. 3a), between the *b*-axis and *T* (Fig. 3b), between the *c*-axis

277 and T (Fig. 3c), and between the β and T (Fig. 3e). As T increases from ~300 to 923 K,
278 our data suggested that the a-axis increases by 0.61(1)%, the b-axis by 0.73(1)%, the c-
279 axis by 1.12(1)%, and the volume by 2.62(1)% (Table 1); the ratio of the relative thermal
280 expansions along the a-, b- and c-axes is 1:1.10:1.84, suggesting that the c-axis is much
281 more expandable than the other two axes. In contrast, the data from Fukuda et al. (1997)
282 suggested that the a-axis increases by 0.61%, the b-axis by 0.65%, the c-axis by 1.02%,
283 and the volume by 2.45% for a similar T interval (from 298 to 918 K). It follows that the
284 volumetric thermal expansion constrained by Fukuda et al. (1997) should be generally
285 smaller than that defined by this study.

286 If the phase transition T from the metastable Lrn to the α'_L phase on heating is
287 assumed to be ~973 K, the extrapolated unit-cell parameters of the Lrn phase at this T are
288 then a = 5.5462 Å, b = 6.8058 Å, c = 9.4156 Å, V = 354.87 Å^3, and β = 93.345°.
289 Compared to the unit-cell parameters of the α'_L phase at 973 K (Table 1), which can be
290 translated as a = 5.532 Å, b = 6.864 Å, c = 9.443 Å, V = 358.53 Å^3, and β = 90° (Saalfeld
291 1975), the relative changes in the unit cells accompanying this phase transition are
292 suddenly a reduction in the a-axis (~0.26%), some expansions of the b-axis (~0.86%), c-
293 axis (~0.29%) and volume (~1.03%), and a huge jump of the β angle. It concludes that
294 this phase transition is indeed of first-order character, in agreement with Barnes et al.
295 (1980), Remy et al. (1997a, 1997b), and Liu et al. (2002).

296 In order to derive the volumetric thermal expansion coefficient, the following
297 equations have been fitted with our T-V data

298 $$V_T = V_0 \exp[\int_0^T \alpha_T dT] \quad (3)$$

299 and

$$\alpha_T = a_0 + a_1 T + a_2 T^{-2} \quad (4),$$

where V_T, V_0 and α_T are the high-T volume, room-T volume and volumetric thermal expansion coefficient at temperature T, respectively. a_0, a_1 and a_2 are the constants obtained in fitting the experimental T-V data. Due to the generally linear relationship observed between the volume and T (Fig. 3), a_1 and a_2 should be close to 0, so that their values have been fixed as zero in our data-fitting process. The obtained parameter is then $a_0 = 4.24(1)\times10^{-5}$ K^{-1}.

Similarly, replacing the volume data in the equations (3) and (4) with the axial dimensions, the axial thermal expansion coefficients can be obtained. Our experimental data yield $a_0 = 1.00(1)\times10^{-5}$ K^{-1} for the a-axis, $a_0 = 1.21(1)\times10^{-5}$ K^{-1} for the b-axis and $a_0 = 1.77(2)\times10^{-5}$ K^{-1} for the c-axis, which are in excellent agreement with those from Remy et al. (1997b; $1.00(10)\times10^{-5}$ K^{-1}, $1.25(10)\times10^{-5}$ K^{-1} and $1.79(15)\times10^{-5}$ K^{-1}, respectively).

The volumetric thermal expansion coefficient of the Lrn phase determined in this study is compared to the results from other studies in Table 2. With the only exception of Fukuda et al. (1997), all other experimental studies have obtained remarkably similar values: for example, they vary slightly from 3.97×10^{-5} K^{-1} to $4.25(14)\times10^{-5}$ K^{-1} when T is ~298 K. The reason why Fukuda et al. (1997) does not agree to other experimental studies is presently unknown. On the other hand, the values obtained with a quasi-harmonic lattice dynamic calculation done by Swamy and Dubrovinsky (1997) and with a thermodynamic optimization method done by Holland and Powell (1998) are significantly smaller. The value constrained with the thermodynamic optimization method done by Swamy and Dubrovinsky (1997), however, is in extraordinarily good agreement with the values from most experimental studies.

323

324 Isothermal bulk modulus

325 High-*P* compression experiments at ambient *T* were conducted up to ~16 GPa for
326 the Lrn. No phase transition was observed, which is in good agreement with Reynard et al.
327 (1997) and Remy et al. (1997b). The X-ray diffraction patterns obtained at *P* higher than
328 ~10 GPa did not show any apparent peak-broadening, which was merely a fortuitous
329 situation; according to Klotz et al. (2009), our pressure medium could only maintain a
330 hydrostatic pressure environment up to about 10 GPa.

331 The unit-cell parameters of the Lrn at different pressures are summarized in Table
332 3 and shown in Fig. 5. All unit-cell parameters vary non-linearly with *P* for the
333 investigated *P* range. As *P* increases from 1 atm to 16.25 GPa, the *a*-axis decreases from
334 5.510(1) to 5.297(4) Å (by 3.87(1)%), the *b*-axis decreases from 6.753(2) to 6.529(1) Å
335 (by 3.32(1)%), the *c*-axis decreases from 9.316(1) to 8.931(2) Å (by 4.14(1)%), the
336 volume decreases from 345.6(1) to 307.7(4) Å (by 10.9(2)%), and the β-angle increases
337 from 94.48(1) to 94.82(2) Å (by 0.36(1)%).

338 In order to determine the isothermal bulk modulus, the third-order Birch-
339 Murnaghan equation of state (BM-EoS; Birch 1947) has been fitted with the *P*-*V* data of
340 the Lrn by a least-squares method:

341 $$P = 3K_T f_E (1+2f_E)^{\frac{5}{2}}[1+\frac{3}{2}(K_T^{'}-4)f_E] \quad (5),$$

342 where *P* is the pressure, K_T the isothermal bulk modulus, $K_T^{'}$ the first pressure derivative
343 of K_T, and f_E the Eulerian definition of finite strain, which is $[(V_0/V)^{2/3}-1]/2$, respectively.
344 In the Eulerian definition of finite strain, V_0 is the volume at zero pressure whereas *V* is

the volume at high pressure. When $K_T^{'}$ is set as 4, the isothermal bulk modulus (K_T) of Lrn is 110.8(8) GPa and the zero-pressure volume is 345.5(1) Å^3. If $K_T^{'}$ is not fixed, the results of our best data-fitting are K_T = 103(2) GPa, $K_T^{'}$ = 5.4(4) and V_0 = 345.6(1) Å^3.

The quality of the derived third-order BM-EoS for the Lrn can be evaluated by using the f_E-F plot (Fig. 6); F is defined as $F \equiv P/[3f_E(1+2f_E)^{5/2}]$. Using F, the third-order BM-EoS can be rewritten as:

$$F = K_T + 3/2K_T(K_T^{'} - 4)f_E \quad (6)$$

so that the slope of the line defined by the experimental data should be equal to $3/2K_T(K_T^{'}-4)$, and the intercept value is the isothermal bulk modulus. Accordingly, a slope of zero means $K_T^{'}$ = 4, a negative slope $K_T^{'} < 4$, and a positive slope $K_T^{'} > 4$. Fig. 3 clearly suggests that the $K_T^{'}$ of the Lrn is larger than 4, in agreement with our P-V data-fitting results detailed in the previous paragraph.

A linearized third-order Birch-Murnaghan equation of state (Angel 2000) was used to obtain the parameters of the equations of state for the crystallographic axes, yielding: a_0 = 5.510(1) Å, $K_{T\text{-}a}$ = 99(5) GPa and $K_{T\text{-}a}^{'}$ = 5.8(10) for the a-axis, b_0 = 6.753(3) Å, $K_{T\text{-}b}$ = 137(7) GPa and $K_{T\text{-}b}^{'}$ = 3.0(1) for the b-axis, and c_0 = 9.316(1) Å, $K_{T\text{-}c}$ = 89(2) GPa and $K_{T\text{-}c}^{'}$ = 5.9(4) for the c-axis. The quality of the derived third-order Birch-Murnaghan equation of state for the axes of the Lrn has been evaluated by using the f_E-F plot as well (Fig. 6).

The geometry parameters of the Lrn phase at zero pressure obtained from the first-principles simulation are summarized in Table 4. As usual, the unit-cell parameters a, b and c calculated by the GGA method are larger (0.63 to 1.16%) whereas those

367 calculated by the LDA method are smaller (–1.75 to –2.16%), compared to the
368 experimental determinations by Tsurumi et al. (1994). Additionally, the unit-cell volume
369 calculated by the GGA method is larger by 2.48% whereas that calculated by the LDA
370 method is smaller by –5.89%. Summarily, both methods reproduce well the unit-cell
371 parameters of the Lrn phase.

372 The unit-cell parameters of the Lrn phase at high pressures predicted by our first-
373 principles simulation are shown along with the experimentally-obtained data in Fig. 5.
374 Compared to the experimentally-determined curves, the curves obtained with the GGA
375 method have slightly steeper slopes whereas those obtained with the LDA method have
376 more gentle slopes, which is normal. In general, the GGA method should yield a lower
377 K_T and the LDA method should yield a higher K_T, with the experimentally-constrained K_T
378 falling in between (Deng et al. 2011). The K_T values obtained by fitting equation (5) with
379 the P-V data essentially meet this expectation: K_T = 92(2) GPa ($K_T^{'}$ = 4.9(5), V_0 = 355.0(1)
380 Å^3; GGA) and K_T = 123(3) GPa ($K_T^{'}$ = 4.4(9), V_0 = 325.94(9) Å^3; LDA). When $K_T^{'}$ is set
381 as 4, K_T = 96(1) GPa (V_0 = 354.8(1) Å^3) and K_T = 124(1) GPa (V_0 = 325.9(6) Å^3) are
382 derived from the data predicted with the GGA method and LDA method, respectively. It
383 concludes that our experimentally-constrained K_T value should be a good approximation
384 to the real K_T value of the Lrn phase.

385 The K_T values of the Lrn phase from different studies are compared in Table 5,
386 with the most of them ranging from ~96 to 124 GPa (with the assumption $K_T^{'}$ = 4).
387 Clearly, the result from Remy et al. (1997b) is the one at odd, which can be adequately
388 explained by their used pressure medium of silicon oil. According to Klotz et al. (2009),
389 silicon oil can maintain a hydrostatic pressure environment at P < 3 GPa only, suggesting

390 the high-*P* data in Remy et al. (1997b; 4.6, 10 and 14.7 GPa) were severely affected by
391 deviatoric stress.

392

393 Heat capacity and entropy

394 We calculated the phonon dispersions and VDoS of the Lrn phase by the first-
395 principles method using density functional perturbation theory; the optimized crystal
396 structure with the LDA method was used in the calculation since the geometries of the Ca
397 polyhedra and Si tetrahedra have been slightly better reproduced with the LDA method
398 (Table 4). The dynamical matrices were computed at 22 wave (q) vectors in the Brillouin
399 zone of the primitive cell, and interpolated to obtain the bulk phonon dispersions. Fig. 7
400 shows the predicted dispersion curves along several symmetry directions and the VDoS.
401 The results of the phonon spectra were used to compute the internal energy (E) and
402 isochoric heat capacity (C_V) as functions of temperature. The temperature dependence of
403 the E was obtained by the following equation,

404 $$E(T) = E_{tot} + E_{ZP} + \int \frac{h\omega}{\exp(\frac{h\omega}{kT}) - 1} F(\omega) d\omega \qquad (7),$$

405 with E_{tot} representing the total electronic energy at 0 K, E_{ZP} the zero point vibrational
406 energy, h the Planck's constant, k the Boltzmann's constant, and $F(\omega)$ the vibrational
407 density of states. We evaluated the E_{ZP} in equation (7) using the following equation,

408 $$E_{ZP} = \tfrac{1}{2} \int F(\omega) h\omega d\omega \qquad (8),$$

409 Furthermore, we approximated the lattice contribution to the C_V with the following
410 equation:

411 $$C_V(T) = k\int \frac{(\frac{h\omega}{kT})^2 \exp(\frac{h\omega}{kT})}{\left[(\frac{h\omega}{kT})^2 - 1\right]^2} F(\omega)d\omega \quad (9).$$

412 The C_V result calculated in this way is shown in Table 6.

413 We calculated the isobaric heat capacity (C_P) by adding an anharmonic effect to
414 the C_V obtained from the above calculations, using the following equation:

415 $$C_P = C_V + \alpha_T^{\,2} K_T V_T T \quad (10),$$

416 where α_T, K_T, and V_T were the thermal expansivity, isothermal bulk modulus, and volume
417 at 1 atm and T K, respectively. For the Lrn phase, $\alpha_T = 4.24(4)\times10^{-5}$ K^{-1} and K_T = 103(2)
418 GPa ($K_T^{'}$ = 5.4(4)). The temperature dependence of K_T has not been experimentally
419 determined, thus assumed as zero in our calculation. V_T at T K was calculated with the
420 following equation:

421 $$V_T = V_{298} \exp(\int_{298}^{T} \alpha_T dT) \quad (11),$$

422 where V_{298} = 51.88 cm^3/mol (Remy et al. 1997b). The calculated C_P values are listed in
423 Table 6, along with the experimental results from Todd (1951) and from Coughlin and
424 O'Brien (1957). Errors of our C_P values were propagated from the uncertainty in the
425 thermal expansion coefficients and isothermal bulk modulus, and they decrease from
426 ~6% at ~10 K to ~0.06% at ~202 K, and then increase to ~0.21% at 1000 K. The
427 calculated C_P data were then expressed using the following polynomial of temperature,

428 $$C_P = k_0 + k_1 T^{-0.5} + k_2 T^{-2} + k_3 T^{-3} + k_4 T + k_5 T^2 + k_6 T^3 \quad (12),$$

429 where C_P was in J mol^{-1} K^{-1} and T in K. In the fitting procedure, the data were divided
430 into three different T intervals, 10-50, 50-293, and 293-1000 K. The C_P equation
431 coefficients for the three T intervals are summarized in Table 7.

Our calculated C_P values are compared in Fig. 8 with the heat capacity measurements by Todd (1951; 52.66-296.48 K) and Coughlin and O'Brien (1957; 406.0-964.6 K). For the T range of 52.66-296.48 K, our C_P data show excellent agreement with those from Todd (1951), with the relative difference quickly decreasing from ~13% at ~51 K to ~1% at ~303 K (Table 6). For the T range of 406.0-964.6 K, our C_P data are also in good agreement with those from Coughlin and O'Brien (1957), with the relative difference varying from ~–2.0% (859 K) to ~1.5% (404 K).

The obtained C_P values have been applied to the calculation of the vibrational entropy at T K using the following equation

$$S_T^0 = \int_0^T \frac{C_P}{T} dT \qquad (13).$$

The vibrational entropy at 298 K (S_{298}^0) calculated from the C_P values in the T range of 0 to 298 K obtained in this study is 129.8(13) J mol^{-1} K^{-1}, in good agreement with the only available value derived from the existing low-T heat capacity measurements, 127.6(8) J mol^{-1} K^{-1} (Todd 1951).

Grüneisen parameter

The Grüneisen parameter is often used to describe the pressure dependences of some thermodynamic, elastic and transport properties which are crucial in the investigation of the deep Earth. It is dimensionless, and varies slowly with P and T, and therefore appears very attractive to geophysicists.

The mode Grüneisen parameters (γ_i) of the Lrn phase (298 K) have been calculated according to the following equation

454 $$\gamma_i = -\frac{\partial \ln \nu_i}{\partial \ln V} = \frac{K_T}{\nu_{0i}}\left(\frac{\partial \nu_i}{\partial P}\right)_T \quad (14),$$

455 where v_{0i} and v_i are the frequencies of the vibration mode i of the Lrn phase at room P
456 and high P, respectively (at ambient T). With the high-P Raman data for the Lrn phase
457 from Reynard et al. (1997) and our bulk modulus determined in this study, we calculate
458 the value of the γ_i of the 20 Raman vibration modes, and find that it varies from ~0 (peaks
459 152 and 520 cm^{-1}) to ~1.90 (peak 255 cm^{-1}), with an arithmetic average of ~0.69(52). The
460 details are summarized in Fig. 9. As expected (Gillet et al. 1991; Fujimori et al. 2002),
461 the γ_i values for the lattice modes are generally larger than those for the internal modes of
462 the SiO_4 tetrahedra.

463 The mode Grüneisen parameters can be cast into a microscopic thermal Grüneisen
464 parameter ($\gamma_{th,1}$) with the following average scheme,

465 $$\gamma_{th,1} = \frac{\sum_i C_{V,i}.\gamma_i}{\sum_i C_{V,i}} \quad (15),$$

466 where $C_{V,i}$ is the contribution of the vibration mode i to the isochoric heat capacity. $C_{V,i}$
467 is estimated on the basis of a harmonic Einstein oscillator,

468 $$C_{V,i} = k.\left(\frac{h\nu_i}{kT}\right)^2 \exp\left(\frac{h\nu_i}{kT}\right) \Big/ \left[\exp\left(\frac{h\nu_i}{kT}\right) - 1\right]^2 \quad (16),$$

469 where h is the Planck's constant, and k the Boltzmann's constant. The $\gamma_{th,1}$ of the Lrn
470 phase attains 0.77(8), about 12% larger than the arithmetic average of the mode
471 Grüneisen parameters.

472 Alternatively, a macroscopic thermal Grüneisen parameter ($\gamma_{th,2}$) can be calculated
473 from the following equation

$$\gamma_{th,2} = \frac{\alpha K_T V_T}{C_V} \quad (17).$$

With all the values of the variables on the right-hand side of equation (17) constrained in this study, we obtained $\gamma_{th,2}$ = 1.80(4) for the Lrn phase at the *P*-*T* condition of 298 K and 1 atm.

Clearly there is a sharp difference (relatively ~ 133%) between the microscopic isothermal Grüneisen parameter $\gamma_{th,1}$ and the macroscopic isothermal Grüneisen parameter $\gamma_{th,2}$ for the Lrn phase, which should by no means exist under ideal circumstance. In the cases of other minerals, the observed difference usually appears up to ~ 25% only (Hofmeister and Mao 2002; Tang et al. 2014). Several factors may account for this prominent difference. Firstly, the pressure medium (a 16:4:1 methanol-ethanol-water mixture) used by Reynard et al. (1997) was not able to maintain a fully hydrostatic pressure environment at P > ~10 GPa (Klotz et al. 2009), which should have led to some overestimate in the P measurements (He et al. 2004). Indeed, the v_t-P curves of the Lrn phase shown by Reynard et al. (1997; their Fig. 7) bended towards the P-axis. This situation was exacerbated by the fact that they only used the data in the P range of 6-16 GPa to derive the P dependence of the Raman frequency, which was thus possibly substantially underestimated. Consequently, all the mode Grüneisen parameters should have been strongly underestimated according to equation (14). Secondly, the factor-group analysis (Piriou and McMillan 1983; Remy et al. 1997a) predicted 84 normal modes for the Lrn phase, with 42 Raman-active modes, 39 infrared-active modes and 3 acoustic modes. Since the number of the Raman peaks observed in Reynard et al. (1997) was limited to 20 only, it is thus possible that the microscopic isothermal Grüneisen parameter $\gamma_{th,1}$ obtained here might have been strongly biased. Thirdly, the polyhedral bulk moduli

497 of the Ca polyhedra and the Si tetrahedron in the Lrn phase should be significantly
498 different (Hazen and Finger 1979), a different conversion and average scheme employing
499 the polyhedral bulk moduli, as the one proposed by Hofmeister and Mao (2002), might be
500 more appropriate than the equations (14) and (15). Fourthly, the assumption of a
501 harmonic Einstein oscillator (equation (16)) might be a poor approximation to the actual
502 chemical bonds in the Lrn phase, and the contribution of an anharmonic component may
503 be significant (Fujimori et al. 2002). Whatever the actual reasons are, more spectroscopic
504 investigation on the Lrn phase is deemed necessary in order to solve the discrepancy
505 between the microscopic isothermal Grüneisen parameter $\gamma_{th,1}$ and the macroscopic
506 isothermal Grüneisen parameter $\gamma_{th,2}$.
507
508
509 **IMPLICATIONS**
510
511 Pure Lrn of large quantity has been successfully synthesized for the first time in
512 its *P*-*T* stability field by using high-*P* experimental technique. Its thermal expansivity has
513 been accurately constrained by some high-*T* X-ray powder diffraction experiments
514 (ambient *P*), and the obtained volumetric thermal expansion coefficient is not very
515 different from that determined with the Lrn metastably formed at ambient *P* (Table 2). In
516 comparison, its experimentally-constrained bulk modulus, verified by supplementary
517 first-principles simulation, is much lower than that obtained from the metastably formed
518 material (Remy et al. 1997b), by ~38% (Table 5). However, the DAC experiments in
519 Remy et al. (1997b) used silicon oil as the pressure medium, which should have resulted

520 in presumably significant overestimation in the *P* values (Klotz et al. 2009) and
521 consequently a nominally larger bulk modulus (He et al. 2004). The discrepancy in the
522 bulk moduli is thus highly possibly irrelevant to any possible difference in the used
523 materials. It follows that the difference in the two materials synthesized in the stability
524 field of Lrn or metastably generated at ambient *P* is too small to have any significant
525 impact on the volumetric thermal expansion coefficients (presumably, the bulk moduli as
526 well). Indeed, both materials were shown as heavily twined (Groves 1983; Kim et al.
527 1992; Wang and Weidner 1994; Remy et al. 1995).

528 Furthermore, the defects (such as twins) and the small amounts of impurities in
529 the Lrn phase (such as 0.32% iron and aluminium oxides and 0.14% magnesia; Todd
530 1951) have insignificant influence on the heat capacity and vibrational entropy. Our first-
531 principles simulation, combined with the newly experimentally-determined volumetric
532 thermal expansion coefficient and bulk modulus, provides an independent examination on
533 the results from the heat capacity measurements carried out with the metastably formed
534 material (Todd 1951; Coughlin and O'Brien 1957). The agreement between the results
535 from these two completely different lines is good (Fig. 8); for example, the relative
536 difference between the values of the standard entropy is ~1.6% only.

537 Lrn has been discovered as tiny inclusions in diamonds originating from the deep
538 interior of the Earth (Joswig et al. 1999; Nasdala et al. 2003; Brenker et al. 2005), which
539 provides a means to explore the *P*-*T* conditions of the diamond formation (or the *P*-*T*
540 condition for trapping the Lrn). Accurate estimates of the volumetric thermal expansion
541 coefficient, bulk modulus and Grüneisen parameter are critical in constraining the
542 remnant pressures of the Lrn inclusions (Ye et al. 2001; Gillet et al. 2002; Joswig et al.

2003; Nasdala et al. 2003). With the formation T of the diamond host independently estimated from some geothermometer or assumed from some typical geotherm, the formation P of the diamond host can be accurately constrained (Barron 2005). According to Kagi et al. (2009), the coexisting of Lrn with other calcium-rich silicates such as Wal and Ttn can be extremely useful, and capable to constrain the formation P without any extra estimate of the formation T, provided the volumetric thermal expansion coefficient, bulk modulus and Grüneisen parameter of the coexisting Wal or Ttn known well.

One exercise has been carried out to constrain the P-T condition for trapping the Lrn inclusions by the diamonds from the Kankan district of Guinea (Fig. 10). Joswig et al. (1999) reported the unit-cell parameters of five Lrn inclusions coexisting with the Ttn phase in four diamonds, which, combined with our third order BM-EoS for Lrn, lead to a remnant pressure of 1.3(3) GPa. Using equation (1) in Kagi et al. (2009), and with the thermal expansion and compressibility data for diamond used by them and those for Lrn from this study, the P-T trajectory for the diamonds to trap the Lrn inclusions has been calculated as

$$P = 0.0057T + 0.17 \qquad (18),$$

where P is in GPa, and T in K (the thick curve in Fig. 10). Clearly, this P-T trajectory locates in the stability field of diamond. Its intersection with the P-T curve for equation (1) indicates a minimum P value of ~9.9 GPa as the inclusion-trapping pressure. Furthermore, the T that the Lrn and Ttn inclusions and the diamond host once experienced is of typical mantle character, suggesting that some portions of the deep mantle have distinct CaO-rich composition but similar T, compared to the normal mantle.

565 The discovery of Lrn and other calcium-rich silicates in some diamonds argues
566 that some portions of the deep interior of the Earth have compositions substantially
567 different to the normal pyrolitic mantle (Ringwood 1975; Joswig et al. 1999; Brenker et
568 al. 2005; Zedgenizov et al. 2014). The enriching process of CaO to concentration levels
569 high enough to stabilize these calcium-rich silicates might have been achieved via deep
570 subduction of the CaO-rich continental crust material into the mantle (Irifune et al. 1994;
571 Liu et al. 2012a). How this material interacts with the regular mantle, how the calcium-
572 rich silicates such as Lrn survive the interaction, what new phases form from the
573 reactions at the *P-T* conditions of the mantle are largely unknown (Joachim et al. 2011,
574 2012). It is believed that the thermodynamic properties of the Lrn phase constrained in
575 this study will shed lights on understanding these possible reactions though.
576
577
578 **ACKNOWLEDGEMENTS**
579
580 We thank the constructive comments from two anonymous reviewers and the
581 editorial handling from Dr. K. Crispin. We are grateful for the suggestions from Dr. K.
582 Putrika on an early version of the manuscript. The in situ X-ray diffraction experiments at
583 high pressures were carried out at the National Synchrotron Light Source (NSLS), which
584 is supported by the U.S. Department of Energy, Division of Materials Sciences and
585 Division of Chemical Sciences under Contract No. DE-AC02-76CH00016. The operation
586 of X17C is supported by COMPRES, the Consortium for Materials Properties Research

in Earth Sciences. This work is financially supported by the Natural Science Foundation of China (Grant No. 41273072 and 41440015).

REFERENCES CITED

Akaogi, M., Yano, Y., Tejima, M., Iijima, M. and Kojitani, H. (2004) High-pressure transitions of diopside and wollastonite: phase equilibria and thermochemistry of $CaMgSi_2O_6$, $CaSiO_3$ and $CaSi_2O_5$-$CaTiSiO_5$. Earth and Planetary Science Letters, 143-144, 145-156.

Angel, R.J. (2001) Equation of state. In R.M. Hazen and R.T. Downs, Eds., High-Temperature and High-Pressure Crystal Chemistry, 41, p. 35-60. Reviews in Mineralogy and Geochemistry, Mineralogical Society of America, Chantilly, Virginia.

Barnes, P., Fentiman, C.H. and Jeffery, J.W. (1980) Structurally related dicalcium silicate phases. Acta Crystallographica, A36, 353-356.

Baroni, S., de Gironcoli, S., Dal Corso, A. and Giannozzi, P. (2001) Phonons and related crystal properties from density-functional perturbation theory. Reviews of Modern Physics, 73, 515-562.

Barron, L.M. (2005) A linear model and topography for the host-inclusion mineral system involving diamond. The Canadian Mineralogist, 43, 203-224.

Birch, F. (1947) Finite elastic strain of cubic crystals. Physical Reviews, 71, 809-924.

609 Bowen, N.L. (1940) Progressive metamorphism of siliceous limestone and dolomite. The
610 Journal of Geology, 48, 225-274.
611 Brenker, F.E., Vincze, L., Vekemans, B., Nasdala, L., Stachel, T., Vollmer, C,. Kersten,
612 M., Somogyi, A., Adams, F., Joswig, W. and Harris, J.W. (2005) Detection of a Ca-
613 rich lithology in the Earth's deep (>300 km) convecting mantle. Earth and
614 Planetary Science Letters, 236, 579-587.
615 Ceperley, D.M. and Alder, B.J. (1980) Ground state of the electron gas by a stochastic
616 method. Physical Review Letters, 45, 566-569.
617 Chang, L., Liu, X., Kojitani, H. and Wang, S. (2013) Vibrational mode analysis and heat
618 capacity calculation of $K_2SiSi_3O_9$-wadeite. Physics and Chemistry of Minerals, 40,
619 563-574.
620 Coughlin, J.P. and O'Brien, C.J. (1957) High temperature heat contents of calcium
621 orthosilicate. Journal of Physical Chemistry, 61, 767-769.
622 Deng, L., Liu, X., Liu, H. and Dong, J. (2010) High-pressure phase relations in the
623 composition of albite $NaAlSi_3O_8$ constrained by an ab initio and quasi-harmonic
624 Debye model, and their implications. Earth and Planetary Science Letters, 298,
625 427-433.
626 Deng, L., Liu, X., Liu, H. and Zhang, Y. (2011) A first-principles study of the phase
627 transition from Holl-I to Holl-II in the composition $KAlSi_3O_8$. American
628 Mineralogist, 96, 974-982.
629 Fujimori, H., Komatsu, H., Ioku, K., Goto, S. and Yoshimura, M. (2002) Anharmonic
630 lattice mode of Ca_2SiO_4: ultraviolet laser Raman spectroscopy at high temperatures.
631 Physical Review B, 66, 064306.

632 Fukuda, K., Maki, I. and Ito, S. (1997) Anisotropic thermal expansion of β-Ca_2SiO_4
633 monoclinic crystal. Journal of the American Ceramic Society, 80, 1595-1598.
634 Gasparik, T., Wolf, K. and Smith, C.M. (1994) Experimental determination of phase
635 relations in the $CaSiO_3$ system from 8 to 15 GPa. American Mineralogist, 79, 1219-
636 1222.
637 Gillet, P., Richet, P., Guyot, F. and Fiquet, G. (1991) High-temperature thermodynamic
638 properties of forsterite. Journal of Geophysical Research, 96, 11805-11816.
639 Gillet, P., Sautter, V., Harris, J., Reynard, B., Harte, B. and Kunz, M. (2002) Raman
640 spectroscopic study of garnet inclusions in diamonds from the mantle transition
641 zone. American Mineralogist, 87, 312-317.
642 Green, D.H. and Ringwood, A.E. (1967) The stability fields of aluminous pyroxene
643 peridotite and garnet peridotite and their relevance in upper mantle structures. Earth
644 and Planetary Science Letters, 3, 151-160.
645 Groves, G.W. (1983) Phase transformations in dicalcium silicate. Journal of Materials
646 Science, 18, 1615-1624.
647 Hammersley, J. (1996) Fit2D report. Europe Synchrotron Radiation Facility, Grenoble,
648 France.
649 Hanic, F., Kamarad, J., Stracelsky, J. and Kapralik (1987) The P-T diagram of Ca_2SiO_4.
650 British Ceramic Transactions and Journal, 86, 194-198.
651 Hazen, R.M. and Finger, L.W. (1979) Bulk modulus-volume relationship for cation-anion
652 polyhedra. Journal of Geophysical Research, 84, 6723-6728.

He, D., Shieh, S.R. and Duffy, T.S. (2004) Strength and equation of state of boron suboxide from radial X-ray diffraction in a diamond cell under nonhydrostatic compression. Physical Review B, 70, 184121.

He, Q., Liu, X., Hu, X., Li, S. and Wang, H. (2011) Solid solution between lead fluorapatite and lead fluorvanadate apatite: mixing behavior, Raman feature and thermal expansivity. Physics and Chemistry of Minerals, 38, 741-752.

He, Q., Liu, X., Hu, X., Deng, L., Chen, Z., Li, B. and Fei, Y. (2012) Solid solutions between lead fluorapatite and lead fluorvanadate apatite: compressibility determined by using a diamond-anvil cell coupled with synchrotron X-ray diffraction. Physics and Chemistry of Minerals, 39, 219-226.

Heinz, D.L., and Jeanloz, R. (1984) The equation of state of the gold calibration standard. Journal of Applied Physics, 55, 885-893.

Hofmeister, A.M. and Mao, H.K. (2002) Redefinition of the mode Grüneisen parameter for polyatomic substances and thermodynamic implications. Proceedings of the National Academy of the Sciences of the United States of America, 99, 559-564.

Hohenberg, P. and Kohn, W. (1964) Inhomogeneous electron gas. Physical Reviews, 136, 864-871.

Holland, T.J.B. and Powell, R. (1998) An internally consistent thermodynamic data set for phases of petrological interest. Journal of Metamorphic Geology, 16, 309-343.

Hu, X., Liu, X., He, Q., Wang, H., Qin, S., Ren, L., Wu, C. and Chang, L. (2011) Thermal expansion of andalusite and sillimanite at ambient pressure: a powder X-ray diffraction study up to 1000^{o}C. Mineralogical Magazine, 75, 363-374.

675 Irifune, T., Susaki, J., Yagi, T. and Sawamoto, H. (1989) Phase transformations in
676 diopside $CaMgSi_2O_6$ at pressures up to 25 GPa. Geophysical Research Letters, 16,
677 187-190.
678 Irifune, T. (1994). Absence of an aluminous phase in the upper part of the Earth's lower
679 mantle. Nature, 370, 131-133.
680 Irifune, T., Ringwood, A.E. and Hibberson, W.O. (1994) Subduction of continental crust
681 and terrigenous and pelagic sediments: an experimental study. Earth and Planetary
682 Science Letters, 117, 101-110.
683 Jackson, I. (1998) Elasticity, composition and temperature of the Earth's lower mantle: a
684 reappraisal. Geophysical Journal International, 134, 291-311.
685 Joachim, B., Gardés, E., Abart, R. and Heinrich, W. (2011) Experimental growth of
686 åkermanite reaction rims between wollastonite and monticellite: evidence for
687 volume diffusion control. Contributions to Mineralogy and Petrology, 161, 389-399.
688 Joachim, B., Gardés, E., Velickov, B., Abart, R. and Heinrich, W. (2012) Experimental
689 growth of diopside + merwinite reaction rims: the effect of water on microstructure
690 development. American Mineralogist, 97, 220-230.
691 Jost, K.H., Ziemer, B. and Seydel, R. (1977) Redetermination of the structure of β-
692 dicalcium silicate. Acta Crystallographica, B33, 1696-1700.
693 Joswig, W., Stachel, T.H., Harris, J.W., Baur, W.H. and Brey, G.P. (1999) New Ca-
694 silicate inclusions in diamonds-tracer from the lower mantle. Earth and Planetary
695 Science Letters, 173, 1-6.

Joswig, W., Paulus, E.F., Winkler, B. and Milman, V. (2003) The crystal structure of $CaSiO_3$-walstromite, a special isomorph of wollastonite-II. Zeitschrift für Kristallographie, 218, 811-818.

Kagi, H., Odake, S., Fukura, S. and Zedgenizov, D.A. (2009) Raman spectroscopic estimation of depth of diamond origin: technical developments and the application. Russian Geology and Geophysics, 50, 1183-1187.

Kanzaki, M., Stebbins, J.F. and Xue, X. (1991) Characterization of quenched high pressure phases in $CaSiO_3$ system by XRD and ^{29}Si NMR. Geophysical Research Letters, 18, 463-466.

Kim, Y.J., Nettleship, I. and Kriven, W.M. (1992) Phase transformations in dicalcium silicate: II, TEM studies of crystallography, microstructure and mechanisms. Journal of the American Ceramic Society, 75, 2407-2419.

Klement, Jr.W. and Cohen, L.H. (1974) Determination of the $\beta \leftrightarrow \alpha'$ transition in Ca_2SiO_4 to 7 kbar. Cement and Concrete Research, 4, 939-943.

Klotz, S., Chervin, J.C., Munsch, P. and Le Marchand, G. (2009) Hydrostatic limits of 11 pressure transmitting media. Journal of Physics D: Applied Physics, 42, 075413.

Kohn, W. and Sham, L.J. (1965) Self-consistent equations including exchange and correlation effects. Physical Reviews, 140, 1133-1138.

Lai, G.C., Nojiri, T. and Nakano, K.I. (1992) Studies of the stability of β-Ca_2SiO_4 doped by minor ions. Cement and Concrete Research, 22, 743-754.

Lee, M.H. (1995) Advanced pseudopotentials for large scale electronic structure calculations. PhD thesis, University of Cambridge, UK.

718 Lin, J.S., Qteish, A., Payne, M.C. and Heine, V. (1993) Optimized and transferable
719 nonlocal separable ab initio pseudopotentials. Physical Review B, 47, 4174-4180.
720 Liu, J., Duan, C.G., Mei, W.N., Smith, R.W. and Hardy, J.R. (2002) Polymorphous
721 transformations in alkaline-earth silicates. Journal of Chemical Physics, 116, 3864-
722 3869.
723 Liu, L. and Ringwood, A.E. (1975) Synthesis of a perovskite-type polymorph of $CaSiO_3$.
724 Earth and Planetary Science Letters, 28, 209-211.
725 Liu, L. (1978) High pressure Ca_2SiO_4, the silicate K_2NiF_4-isotype with crystalchemical
726 and geophysical implications. Physics and Chemistry of Minerals, 3, 291-299.
727 Liu, X., He, Q., Wang, H., Fleet, M.E. and Hu, X. (2010) Thermal expansion of kyanite
728 at ambient pressure: an X-ray powder diffraction study up to 1000^{o}C. Geoscience
729 Frontiers, 1, 91-97.
730 Liu, X., Shieh, S.R., Fleet, M.E., Zhang, L. and He Q. (2011) Equation of state of
731 carbonated hydroxylapatite at ambient temperature up to 10 GPa: significance of
732 carbonate. American Mineralogist, 96, 74-80.
733 Liu, X., Ohfuji, H., Nishiyama, N., He, Q., Sanehira, T. and Irifune T. (2012a) High-P
734 behavior of anorthite composition and some phase relations of the CaO-Al_2O_3-SiO_2
735 system to the lower mantle of the Earth, and their geophysical implications. Journal
736 of Geophysical Research, 117, B09205.
737 Liu, X., Chen, J., Tang, J., He, Q., Li, S., Peng, F., He, D., Zhang, L. and Fei, Y. (2012b)
738 A large volume cubic press with a pressure-generating capability up to about 10
739 GPa. High Pressure Research, 40, 239-254.

Liu, X., Wang, S., He, Q., Chen, J., Wang, H., Li, S., Peng, F., Zhang, L. and Fei Y (2012c) Thermal elastic behavior of $CaSiO_3$-walstromite: a powder X-ray diffraction study up to 900°C. American Mineralogist, 97, 262-267.

Mason, B. (1957) Larnite, scawtite, and hydrogrossular from Tokatoka, New Zealand. American Mineralogist, 42, 379-392.

Mao, H.K., Yagi, T. and Bell, P.M. (1977) Mineralogy of the Earth's deep mantle: quenching experiments on mineral compositions at high pressure and temperature. Carnegie Institution of Washington Yearbook, 76, 502-504.

Mao, H.K., Bell, P.M., Shaner, J.W. and Steinberg, D.J. (1978) Specific volume measurements of Cu, Mo, Pt, and Au and calibration of ruby R1 fluorescence pressure gauge for 0.006 to 1 Mbar. Journal of Applied Physics, 49, 3276-3283.

Monkhorst, H.J. and Pack, J.D. (1976) Special points for Brillouin-zone integrations. Physical Review B, 13, 5188-5192.

Nasdala, L., Brenker, F.E., Glinnemann, J., Hofmeister, W., Gasparik, T., Harris, J.W., Stachel, T. and Reese, I. (2003) Spectroscopic 2D-tomography: residual pressure and strain around mineral inclusions in diamonds. European Journal of Mineralogy, 15, 931-935.

Payne, M.C., Teter, M.P., Allan, D.C., Arias, T.A. and Joannopoulos, J.D. (1992) Iterative minimization techniques for ab initio total-energy calculations: molecular dynamics and conjugate gradients. Review of Modern Physics, 64, 1045-1097.

Perdew, J.P. and Zunger, A. (1981) Self-interaction correction to density-functional approximations for many-electron systems. Physical Review B, 23, 5048-5079.

762 Perdew, J.P., Burke, K. and Ernzerhof, M. (1996) Generalized gradient approximation
763 made simple. Physical Review Letters, 77, 3865-3868.
764 Piriou, B. and McMillan, P. (1983) The high-frequency vibrational spectra of vitreous
765 and crystalline orthosilicates. American Mineralogist, 68, 426-443.
766 Refson, K., Tulip, P.R. and Clark, S.J. (2006) Variational density-functional perturbation
767 theory for dielectrics and lattice dynamics. Physical Review B, 73, 155114.
768 Remy, C., Guyot, F. and Madon, M. (1995) High pressure polymorphism of dicalcium
769 Ca_2SiO_4. A transmission electron microprobe study. Physics and Chemistry of
770 Minerals, 22, 419-427.
771 Remy, C., Reynard, B. and Madon, M. (1997a) Raman spectroscopic investigations of
772 dicalcium silicate: polymorphs and high-temperature phase transformations. Journal
773 of the American Ceramic Society, 80, 413-423.
774 Remy, C., Andrault, D. and Madon, M. (1997b) High-temperature, high-pressure X-ray
775 investigation of dicalcium silicate. Journal of the American Ceramic Society, 80,
776 851-860.
777 Reynard, B., Remy, C. and Takir, F. (1997) High-pressure Raman spectroscopic study of
778 Mn_2GeO_4, Ca_2GeO_4, Ca_2SiO_4, and $CaMgGeO_4$ olivines. Physics and Chemistry of
779 Minerals, 24, 77-84.
780 Ringwood, A.E. (1975) Composition and Petrology of the Earth's Mantle. McGraw-Hill,
781 New York.
782 Rodrigues, F.A. (2003) Synthesis of chemically and structurally modified dicalcium
783 silicate. Cement and Concrete Research, 33, 823-827.

784 Saalfeld, H. (1975) X-ray investigation of single crystals of β-Ca_2SiO_4 (larnite) at high
785 temperatures. American Mineralogist, 60, 824-827.
786 Sueda, Y., Irifune, T., Yamada, A., Inoue, T., Liu, X. and Funakoshi, K. (2006) The
787 phase boundary between $CaSiO_3$ perovskite and Ca_2SiO_4 + $CaSi_2O_5$ determined by
788 in situ X-ray observations. Geophysical Research Letters, 33, L10307.
789 Swamy, V. and Dubrovinsky, L.S. (1997) Thermodynamic data for the phases in the
790 $CaSiO_3$ system. Geochimica et Cosmochimica Acta, 61, 1181-1191.
791 Takahashi, E. (1986) Melting of a dry peridotite KLB-1 up to 14 GPa: implications on the
792 origin of peridotitic upper mantle. Journal of Geophysical Research, 91, 9367-9382.
793 Tang, J., Liu, X., Xiong, Z., He, Q., Shieh, R.S. and Wang, H. (2014) High temperature
794 X-ray diffraction, DSC-TGA, polarized FTIR and high pressure Raman
795 spectroscopy studies on euclase. Bulletin of Mineralogy, Petrology and
796 Geochemistry, 33, 289-298.
797 Tilley, C.E. (1929) On larnite (calcium orthosilicate, a new mineral) and its associated
798 minerals from the limestone contact-zone of Scawt Hill, Co. Antrim. Mineralogical
799 Magazine, 22, 77-86.
800 Tilley, C.E. (1947) The gabbro-limestone contact of Camas Mor, Muck, Inverness-shire.
801 Bulletin de la Commission Geologique de Finlande, 140, 97-106.
802 Tilley, C.E. (1951) A note on the progressive metamorphism of siliceous limestones and
803 dolomites. Geological Magazine, 88, 175-178.
804 Todd, S.S. (1951) Low-temperature heat capacities and entropies at 298.16 ^{o}K of
805 crystalline calcium orthosilicate, zinc orthosilicate and tricalcium silicate. Journal
806 of the American Chemical Society, 73, 3277-3278.

807 Thompson, A.B. (1992) Water in the Earth's upper mantle. Nature, 358, 295-302.

808 Tsurumi, T., Hirano, Y., Kato, H., Kamiya, T. and Daimon, M. (1994) Crystal structure
809 and hydration of belite. Ceramic Transactions, 40, 19-25.

810 Wang, S., Liu, X., Fei, Y., He, Q. and Wang, H. (2012) In situ high-temperature powder
811 X-ray diffraction study on the spinel solid solutions $(Mg_{1-x}Mn_x)Cr_2O_4$. Physics and
812 Chemistry of Minerals, 39, 189-198.

813 Wang, Y. and Weidner, D.J. (1994) Thermoelasticity of $CaSiO_3$ perovskite and
814 implications for the lower mantle. Geophysical Research Letters, 21, 895-898.

815 Xiong, Z., Liu, X., Shieh, S.R., Wang, F., Wu, X., Hong, X. and Shi, Y. (2015) Equation
816 of state of a synthetic ulvöspinel, $(Fe_{1.94}Ti_{0.03})Ti_{1.00}O_{4.00}$, at ambient temperature.
817 Physics and Chemistry of Minerals, 42, 171-177.

818 Yamnova, N.A., Zubkova, N.V., Eremin, N.N., Zadov, A.E. and Gazeev, V.M. (2011)
819 Crystal structure of larnite β-Ca_2SiO_4 and specific features of polymorphic
820 transitions in dicalcium orthosilicate. Crystallography Reports, 56, 210-220.

821 Yannaquis, N. and Guinier, A. (1959) La transition polymorphique β-γ de l'orthosilicate
822 de calcium. Bulletin de la Societe Francaise de Mineralogie et de Cristallographie,
823 82, 126-136.

824 Ye, K., Liou, J.B., Cong, B. And Maruyama, S. (2001) Overpressures induced by coesite-
825 quartz transition in zircon. American Mineralogist, 86, 1151-1155.

826 Zedgenizov, D. A., Shatskiy, A., Ragozin, A. L., Kagi, H. and Shatsky V.S. (2014)
827 Merwinite in diamond from Sao Luiz, Brazil: a new mineral of the Ca-rich mantle
828 environment. American Mineralogist, 99, 547-550.

829

Figure Captions

FIGURE 1. Phase diagram of composition Ca_2SiO_4: (a) Phase diagram at 1 atm (*T* in K); (b) Phase diagram at high-*P* and high-*T* conditions (H*P*-H*T*). The phase sequence in (a) is from Remy et al. (1997a). The solid univariant curves of $\gamma = \beta$, $\gamma = \alpha'_L$ and $\beta = \alpha'_L$ in (b) are from Remy et al. (1995). The solid circle in (b) represents the *P*-*T* condition of our Lrn-synthesizing experiments, which locates in the stability field of the Lrn phase, but near the high *P*-*T* extension of the $\beta = \alpha'_L$ univariant curve. In addition, Liu (1978) observed a K_2NiF_4-structured Ca_2SiO_4 phase at ~24 GPa and 1273 K, and Wang and Weidner (1994) detected the phase transition between the β phase and the α'_L phase at ~9 GPa and 1350 K.

FIGURE 2. XRD patterns collected at (a) 300 K, (b) 923 K, and (c) 973 K (ambient *P*). The material underwent the phase transition from the β phase to the α'_L phase at a temperature between 923 and 973 K. A few weak peaks, as indicated by the asterisks, do not belong to the Lrn phase, but are attributable to the γ phase, which might have been generated during the sample-grinding process. The relative intensities of these weak peaks did not change as the experimental *T* increased, suggesting that the volume proportion of the γ phase did not increase and the potential phase transition from the metastable Lrn to the γ phase did not actually take place at low temperatures (Fig. 1a).

852 **FIGURE 3.** Variation of the unit-cell parameters of Lrn with T (ambient P): (a) the a-
853 axis; (b) the b-axis; (c) the c-axis; (d) the volume; (e) the angle β. Note that lengths
854 of the error bars are generally equal to or smaller than the symbols.
855
856 **FIGURE 4.** XRD patterns of Lrn collected at 3.80, 7.61, 12.30 and 16.25 GPa (ambient
857 T). Note that peak broadening at $P > 10$ GPa was not obvious.
858
859 **FIGURE 5.** Variation of the unit-cell parameters of Lrn with P (ambient T for the
860 experimental data whereas zero T for the simulated data): (a) the a-axis; (b) the b-
861 axis; (c) the c-axis; (d) the volume; (e) the angle β. Note that lengths of the error
862 bars of the experimental data are generally equal to or smaller than the symbols.
863 The curves, both solid and broken, are drawn according to the derived third order
864 BM-EoS.
865
866 **FIGURE 6.** Eulerian strain-normalized pressure (f_E-F) plots based on the BM-EoS
867 (experimental data only): (a) is for the a-axis; (b) is for the b-axis; (c) is for the c-
868 axis; (d) is for the volume. Estimated standard deviations were calculated following
869 the method in Heinz and Jeanloz (1984). The solid lines are the weighted linear fits
870 through the data.
871
872 **FIGURE 7.** Phonon dispersions and VDoS of Lrn (LDA).
873

874 **FIGURE 8.** Isobaric heat capacity of Lrn. Our C_V results from the first-principles method
875 were combined with our experimentally-determined volumetric thermal expansion
876 coefficient and isothermal bulk modulus to derive the C_P values.
877
878 **FIGURE 9.** Isothermal mode Grüneisen parameters (γ_i) of Lrn (ambient T). High-P
879 Raman data used in the calculation are from Reynard et al. (1997). Although a full
880 assignment of the Raman-active vibrations of Lrn has not been available, it is
881 generally appropriate to assign the peaks with $\nu_i > \sim 500$ cm^{-1} as the internal modes
882 of the SiO_4 tetrahedra and the peaks at lower frequencies as the lattice modes
883 (Remy et al. 1997a).
884
885 **FIGURE 10.** *P-T* trajectory for trapping the Lrn inclusion by the diamonds from the
886 Kankan district of Guinea (thick curve). The *P-T* profiles of the cold slab and hot
887 slab are sketched from Thompson (1992), and the *P-T* profile for the normal mantle
888 follows the 1600 K adiabat for the simplified pyrolite composition in Jackson
889 (1998). Since the Lrn inclusion always coexists with the Ttn phase (Joswig et al.
890 1999), the phase boundaries between Wal and Lrn + Ttn (equation 1), and between
891 Lrn + Ttn and CaPv (equation 2) are plotted to show the stability field of the phase
892 assemblage Lrn + Ttn (Gasparik et al. 1994; Sueda et al. 2006). The well known
893 phase boundary of graphite and diamond is also sketched.

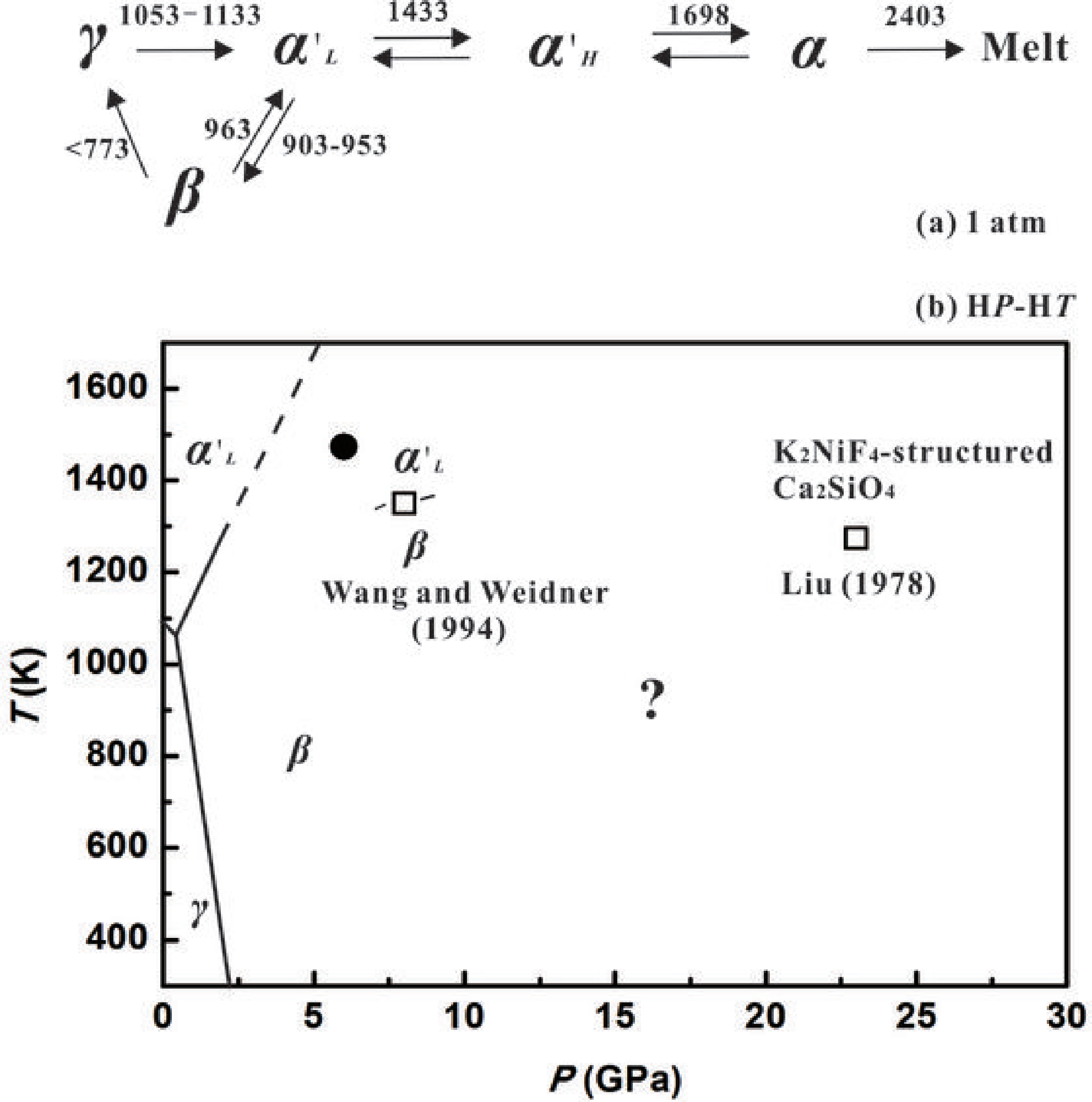
γ
1053−1133
α'L
1433
α'H
1698
α
2403
Melt
<773
963
903-953
β
(a) 1 atm
(b) HP-HT
1600
1400
1200
1000
800
600
400
T(K)
α'L
α'L
β
Wang and Weidner
(1994)
K2NiF4-structured
Ca2SiO4
Liu (1978)
?
β
γ
0
5
10
15
20
25
30
P (GPa)

Figure 1 of Xiong et al. (2015)

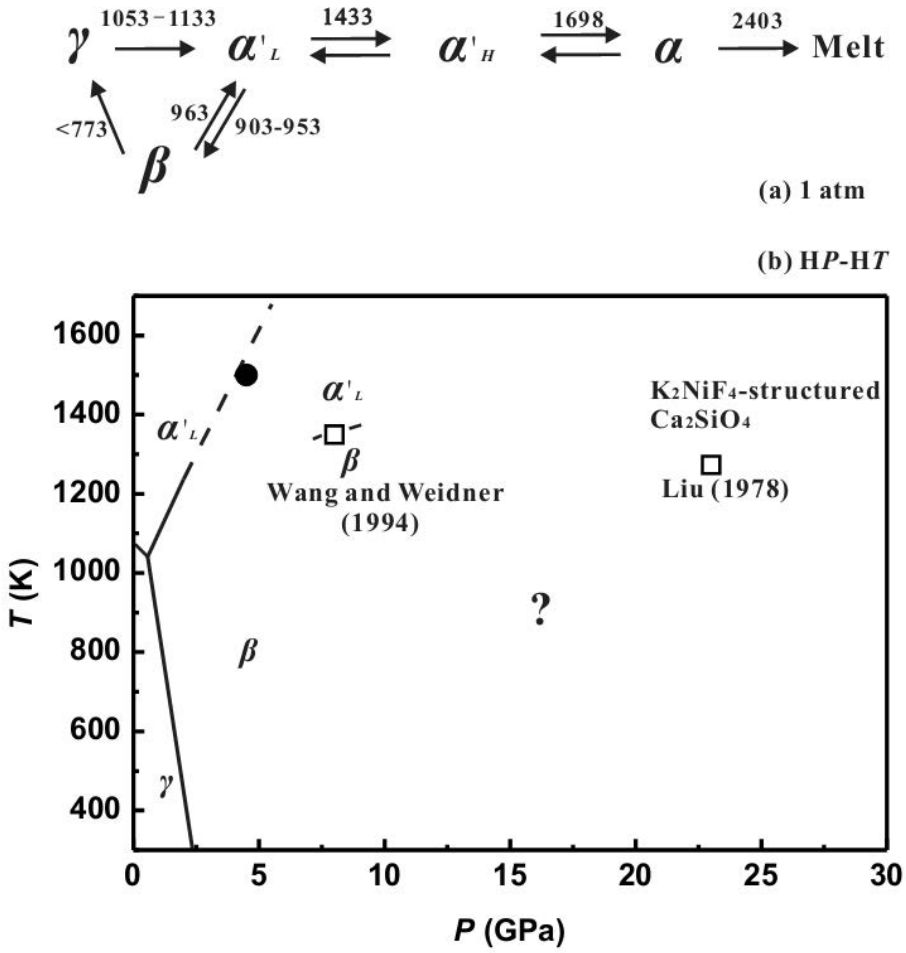

Figure 2 of Xiong et al. (2015)

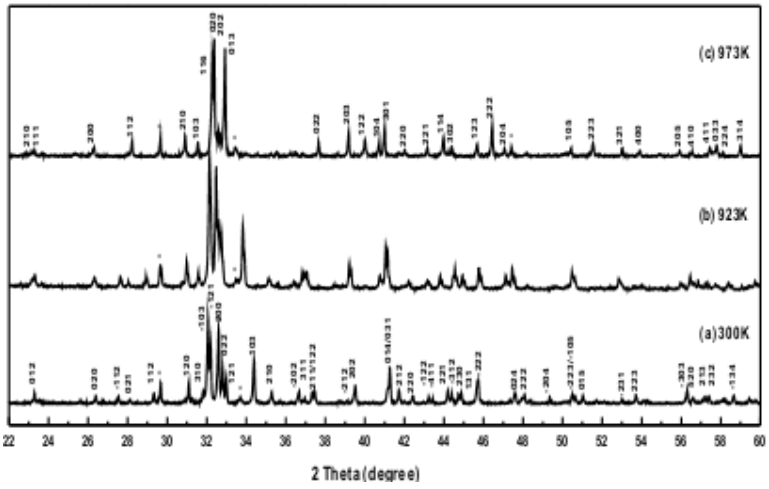

Figure 3 of Xiong et al. (2015)

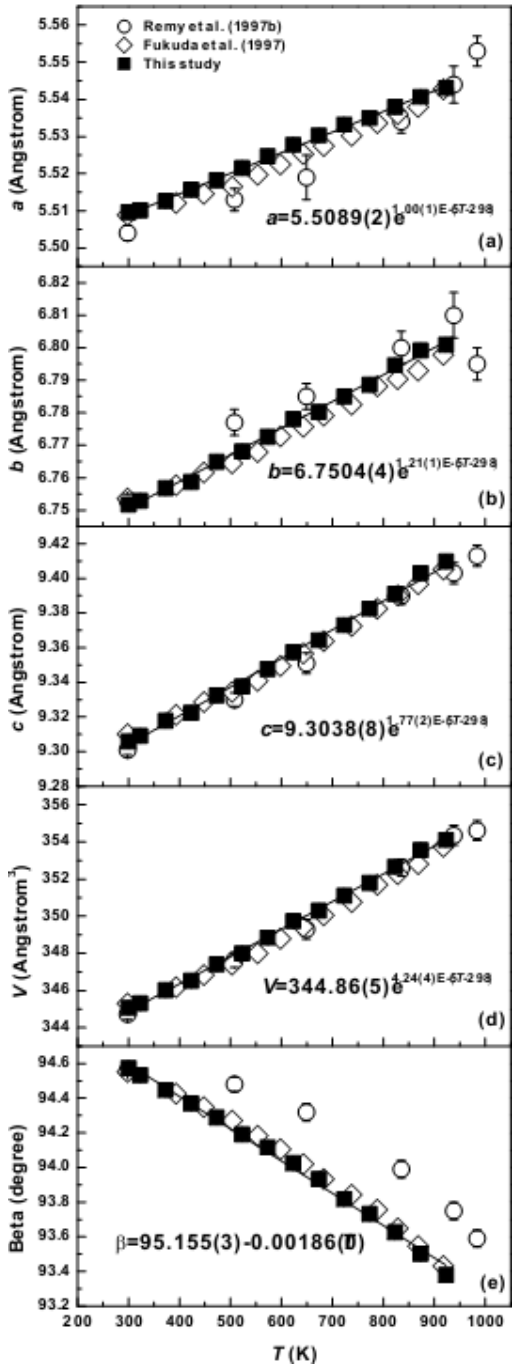

Figure 4 of Xiong et al. (2015)

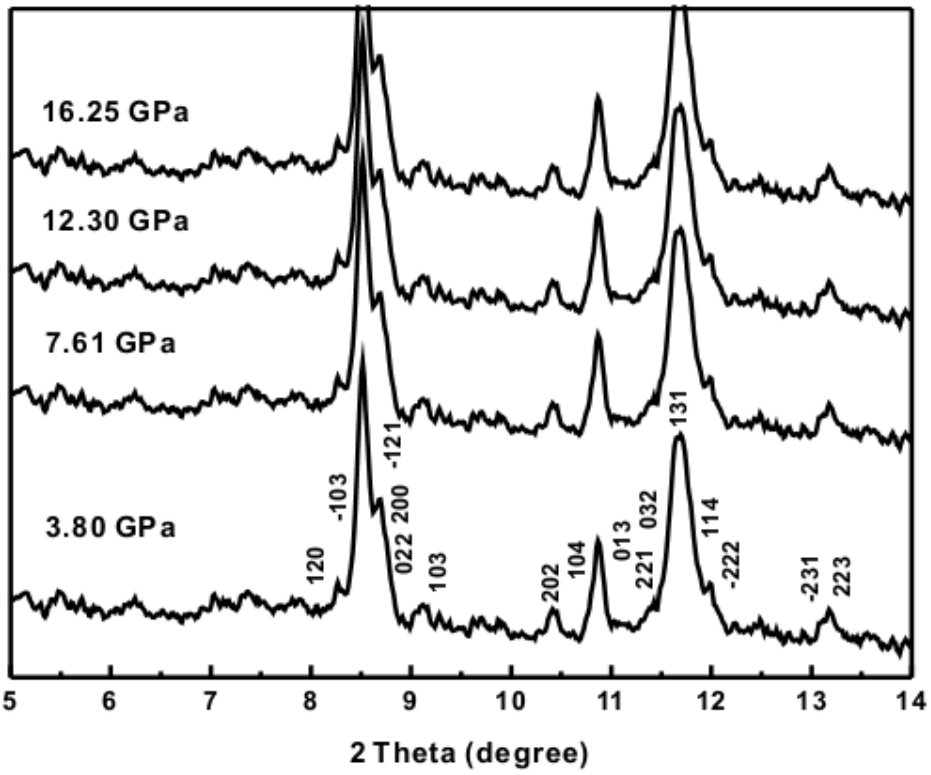

Figure 5 of Xiong et al. (2015)

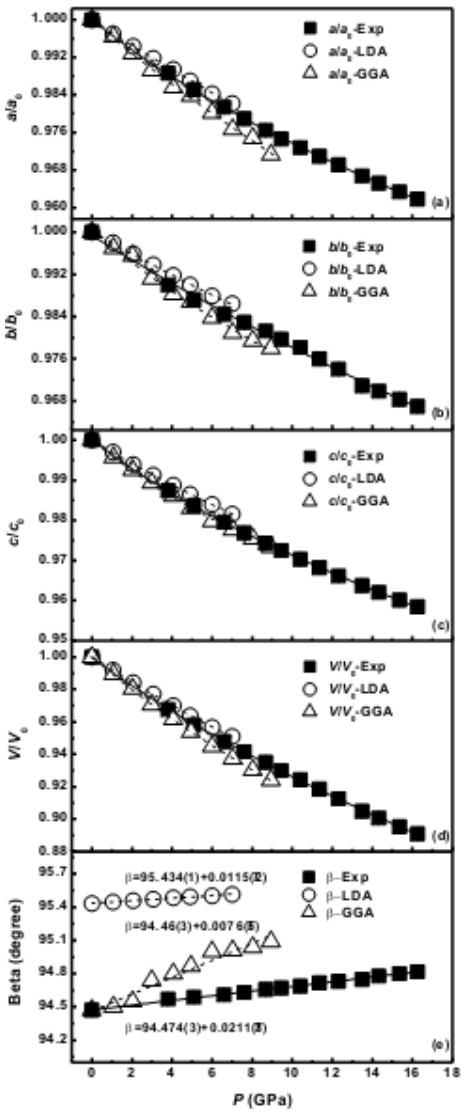

Figure 6 of Xiong et al. (2015)

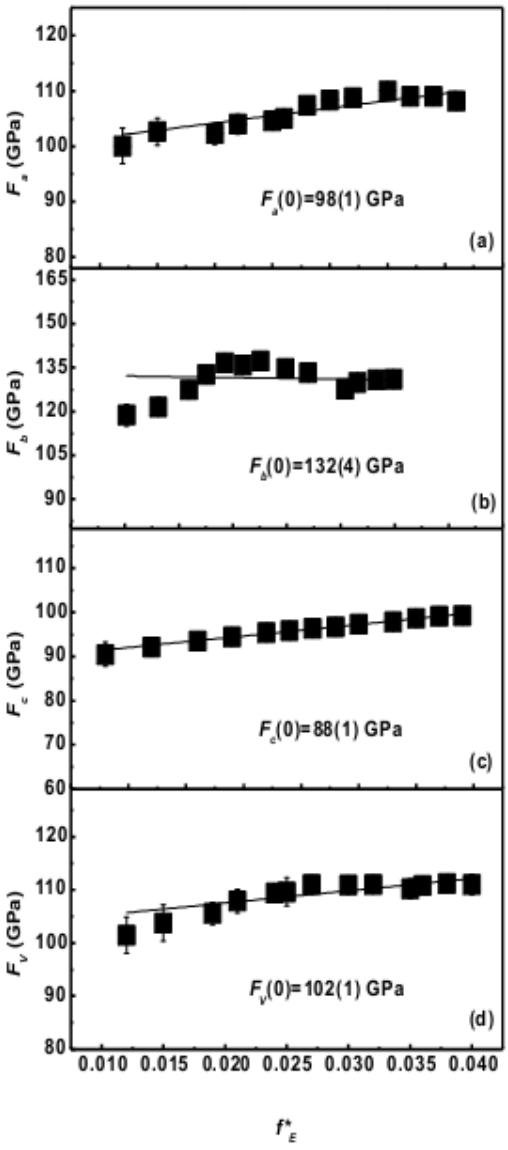

Figure 7 of Xiong et al. (2015)

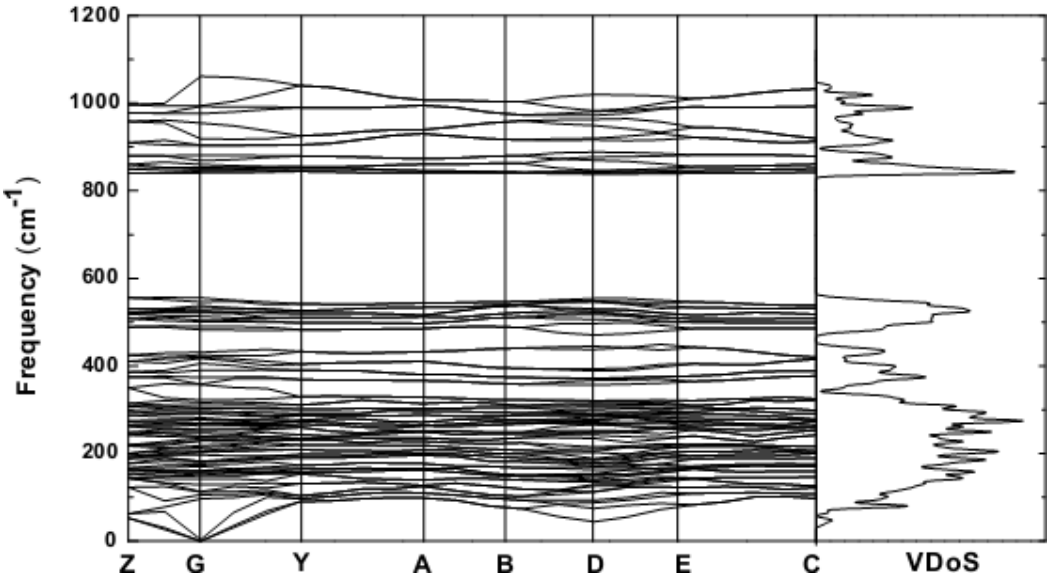

Figure 8 of Xiong et al. (2015)

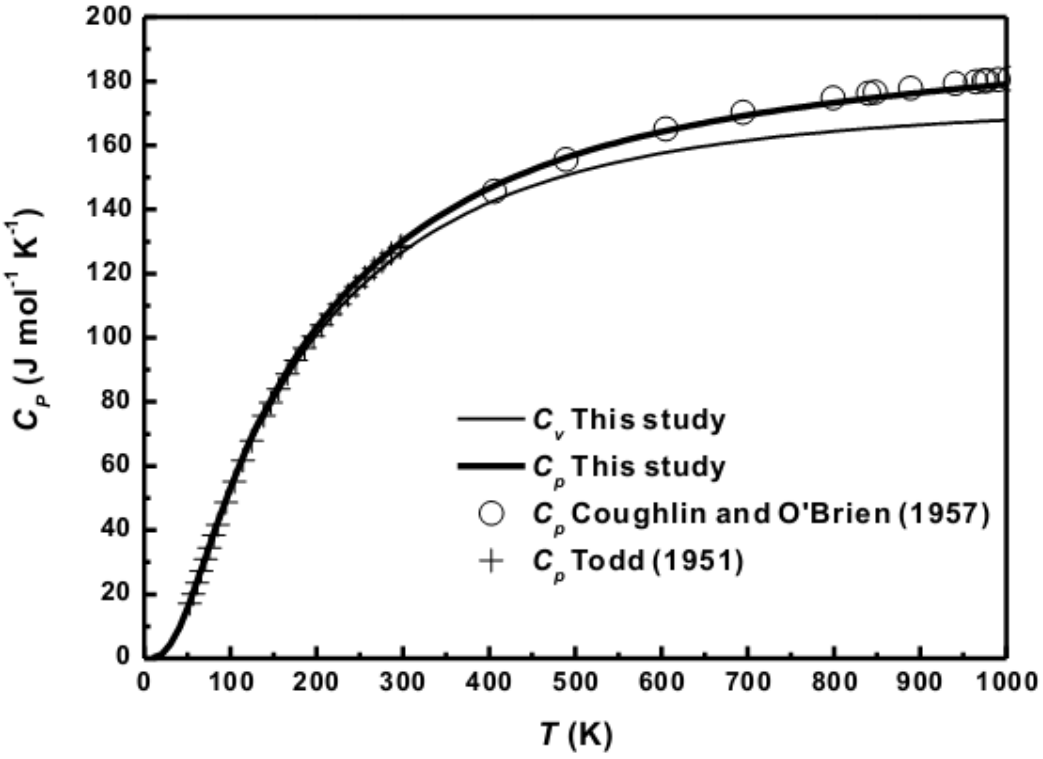

Figure 9 of Xiong et al. (2015)

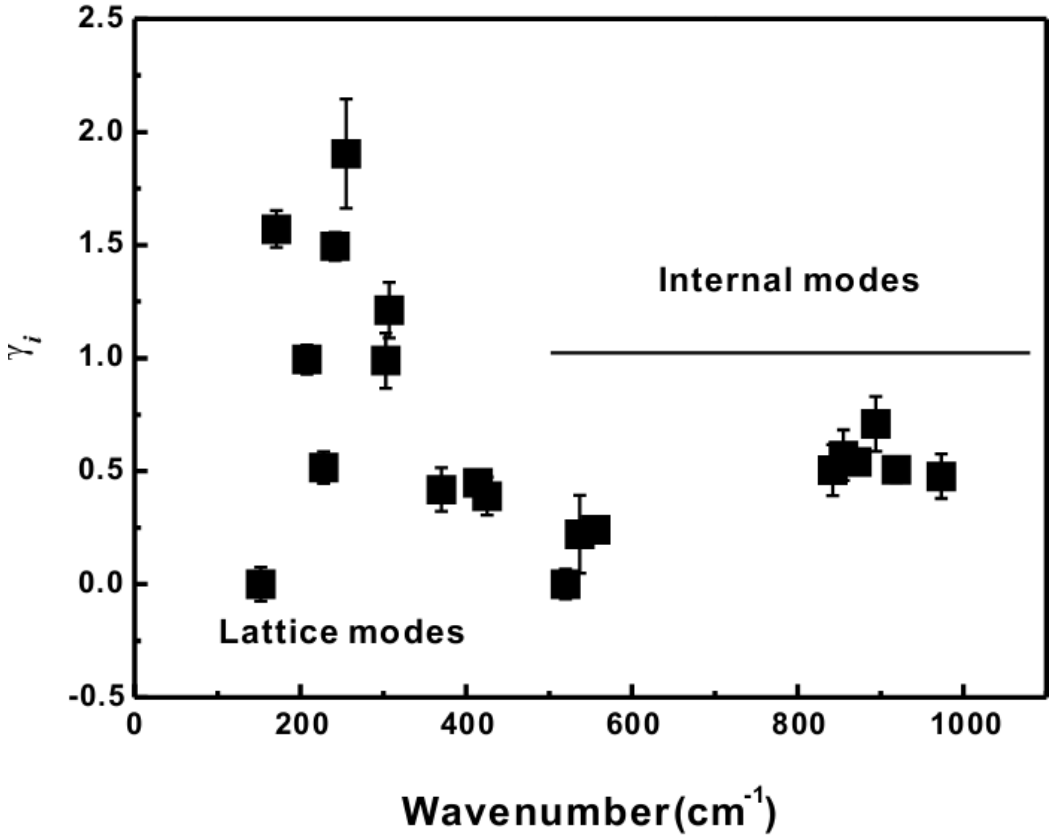

Fig. 10 of Xiong et al. (2015)

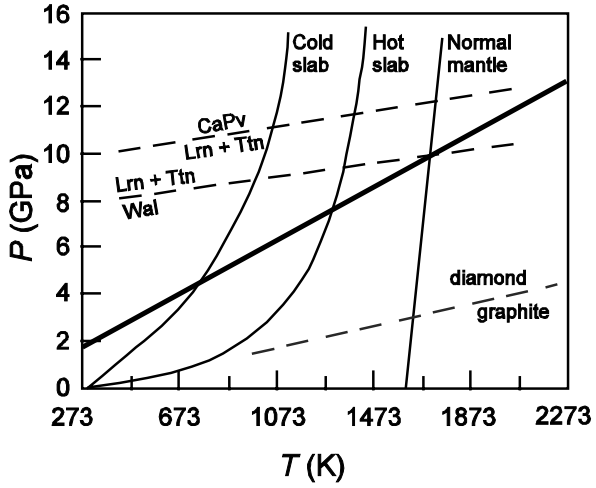

TABLE 1. Unit-cell parameters of Lrn and α'_L versus T (ambient P)

T (K)	a (Å)	b (Å)	c (Å)	β (º)	V (Å^3)
Lrn					
300	5.5096(4)*	6.7518(4)	9.3059(8)	94.575(7)	345.07(19)
323	5.5101(2)	6.7529(2)	9.3091(4)	94.533(4)	345.31(11)
373	5.5126(2)	6.7567(2)	9.3178(4)	94.447(3)	346.02(9)
423	5.5157(2)	6.7587(3)	9.3223(5)	94.369(4)	346.52(13)
473	5.5183(2)	6.7649(2)	9.3324(3)	94.289(3)	347.41(9)
523	5.5214(2)	6.7681(3)	9.3377(5)	94.191(5)	348.01(13)
573	5.5246(3)	6.7726(3)	9.3476(7)	94.117(6)	348.85(17)
623	5.5278(3)	6.7781(3)	9.3575(7)	94.025(6)	349.74(15)
673	5.5303(3)	6.7801(4)	9.3643(8)	93.934(7)	350.31(17)
723	5.5332(2)	6.7851(3)	9.3731(6)	93.818(5)	351.11(14)
773	5.5351(2)	6.7887(3)	9.3826(6)	93.731(4)	351.81(11)
823	5.5379(2)	6.7946(2)	9.3912(5)	93.626(4)	352.67(9)
873	5.5407(4)	6.7992(5)	9.4031(9)	93.502(6)	353.57(15)
923	5.5431(2)	6.8009(4)	9.4098(8)	93.379(6)	354.11(12)
α'_L					
973	5.532(3)	20.591(16)	9.443(6)	-	1075.6(12)
1023	5.764(4)	21.019(11)	9.855(4)	-	1193.9(11)

*Number in the parentheses represents one standard deviation in the rightmost digit.

TABLE 2. Volumetric thermal expansion coefficients of Lrn (ambient P)[*]

T range (K)	a_0 (10^{-5})	a_1 (10^{-9})	Data source	Note
300-923	4.24(4)	-	This study	powder XRD
298-984	4.25(14)	-	Remy et al. (1997b)	powder XRD
298-918	2.87(15)	35(4)	Fukuda et al. (1997)	powder XRD
293, 993[†]	3.97	-	Barnes et al. (1980)	powder XRD
298	1.80	-	Swamy and Dubrovinsky (1997)	QHLDC[‡]
298-923	2.38(3)	17.8(9)	Holland and Powell (1998)	TOE[§]
-	4.11(0)	15.4(0)	Swamy and Dubrovinsky (1997)	TOE[§]

[*] $\alpha_T = a_0 + a_1(T\text{-}T_0) + a_2(T\text{-}T_0)^{-2}$, where α_T and a_0 are in K^{-1}, a_1 is in K^{-2}, and a_2 (always zero in the case of Lrn) is in K. T_0 is set as 298 K.

[†] The reported unit-cell parameters at 293 and 993 K were used in the calculation.

[‡] Quasi-Harmonic Lattice Dynamic Calculation done with the GEMIN algorithm.

[§] Thermodynamically Optimized Estimate.

TABLE 3. Unit-cell parameters of Lrn versus *P* (ambient *T*)

P (GPa)	*a* (Å)	*b* (Å)	*c* (Å)	*β* (°)	*V* (Å^3)
0.0001(1)	5.510(1)*	6.753(2)	9.316(1)	94.48(1)	345.6(1)
3.80(10)†	5.446(6)	6.685(6)	9.197(2)	94.57(2)	333.7(1)
5.09 (10)	5.428(5)	6.666(6)	9.163(2)	94.59(4)	330.5(3)
6.60(10)	5.406(3)	6.647(6)	9.125(2)	94.61(2)	326.8(1)
7.61(10)	5.394(7)	6.637(7)	9.101(6)	94.63(3)	324.7(2)
8.68(10)	5.380(6)	6.626(5)	9.078(2)	94.66(2)	322.5(1)
9.45(10)	5.371(5)	6.615(1)	9.061(2)	94.67(2)	320.9(4)
10.39(10)	5.362(6)	6.605(4)	9.041(5)	94.69(5)	319.1(1)
11.35(10)	5.351(4)	6.591(7)	9.021(2)	94.72(2)	317.1(2)
12.30(10)	5.341(5)	6.577(6)	9.003(2)	94.73(2)	315.2(1)
13.49(10)	5.329(4)	6.556(1)	8.980(8)	94.75(3)	312.7(3)
14.33(10)	5.319(4)	6.549(1)	8.965(2)	94.78(2)	311.2(1)
15.35(10)	5.308(2)	6.538(4)	8.947(1)	94.80(1)	309.4(1)
16.25(10)	5.297(4)	6.529(1)	8.931(2)	94.82(2)	307.7(4)

*The number in the parentheses represents one standard deviation in the rightmost digit.

†Uncertainty in the *P* measurement at high *P* assumed to be 0.1 GPa.

TABLE 4. Comparison between experimental and energy-optimized crystallographic data of Lrn

Parameters	Experimental*	Calculated by first-principles simulation			
		LDA	R. D. (%)†	GGA	R. D. (%)†
a(Å)	5.5041	5.4080	-1.75	5.5678	1.16
b(Å)	6.7622	6.6310	-1.94	6.8103	0.71
c(Å)	9.3281	9.1270	-2.16	9.3873	0.63
β(°)	94.172	95.433	1.34	94.466	0.31
V(Å^3)	346.27	325.87	-5.89	354.87	2.48
Ca polyhedron					
Ca1-O1(Å)	2.719	2.682	-1.02	2.752	1.2
Ca1-O2(Å)	2.671	2.672	0.04	2.685	0.55
Ca1-O3(Å)	2.459	2.456	-0.09	2.451	-0.32
Ca1-O4(Å)	2.508	2.482	-1.01	2.513	0.22
Ca2-O1(Å)	2.255	2.238	-0.77	2.280	1.12
Ca2-O2(Å)	2.432	2.418	-0.57	2.464	1.31
Ca2-O3(Å)	2.871	2.856	-0.53	2.907	1.26
Ca2-O4(Å)	2.735	2.737	0.04	2.774	1.41
Si tetrahedron					
Si-O1(Å)	1.598	1.562	-2.23	1.617	1.21
Si-O2(Å)	1.533	1.512	-1.33	1.553	1.34
Si-O3(Å)	1.470	1.457	-0.89	1.486	1.10
Si-O4(Å)	1.672	1.660	-0.69	1.692	1.22
O1- Si-O2(°)	109.051	108.092	-0.88	109.891	0.77
O1-Si-O3(°)	114.907	114.187	-0.62	115.101	0.17
O1-Si-O4(°)	104.195	103.581	-0.59	105.373	1.13
O2-Si-O3(°)	112.622	112.701	0.07	113.343	0.64
O2-Si-O4(°)	99.790	99.840	0.05	99.900	0.11
O3-Si-O4(°)	114.932	114.161	-0.67	114.403	-0.46

*Tsurumi et al. (1994).

†Relative Difference.

TABLE 5. Isothermal bulk modulus (K_T) of Lrn (ambient P)

K_T (GPa)	K_T'	Method	Data source
114(1)	4*	Powder XRD	This study
103(2)	5.4(4)	Powder XRD	This study
166(15)	4*	Powder XRD	Remy et al. (1997b)
124(1)	4*	First-principles simulation (LDA)	This study
123(3)	4.4(9)	First-principles simulation (LDA)	This study
96(1)	4*	First-principles simulation (GGA)	This study
92(2)	4.9(5)	First-principles simulation (GGA)	This study
119	4*	QHLDAC†	Swamy and Dubrovinsky (1997)
119	4*	Thermodynamic optimization	Swamy and Dubrovinsky (1997)
120	4*	Thermodynamic optimization	Holland and Powell (1998)

* K_T' is set as 4.

†Quasi-Harmonic Lattice Dynamic Calculation done with the GEMIN algorithm.

TABLE 6. Heat capacity (J mol^{-1} K^{-1}) of Lrn at selected T

T (K)	Calculated by First-principles*		Experimental†	Experimental‡
	C_V	C_P	C_P	C_P
10	0.06	0.17(1)		
20	1.05	1.26(1)		
30	4.08	4.38(1)		
41	9.16	9.56(1)		
51	15.72	16.23(2)	14.36	-
101	52.91	53.93(4)	53.05	-
152	81.59	83.12(6)	81.75	-
202	101.69	103.73(6)	102.60	-
253	116.37	118.92(9)	117.73	-
303	127.46	130.52(11)	129.29	-
354	135.99	139.56(13)		-
404	142.61	147.69(15)		145.50
455	147.80	151.35(16)		151.91
505	151.91	157.01(19)		157.20
556	155.20	160.81(21)		161.59
606	157.86	163.98(22)		165.25
657	160.03	166.67(24)		168.34
707	161.83	168.97(26)		170.98
758	163.32	170.98(28)		173.24
808	164.58	172.75(30)		175.21
859	165.65	174.32(32)		177.94
909	166.56	175.74(34)		178.46
950	167.19	176.79(35)		179.56
1000	167.89	177.99(37)		180.79

*This work.

†Todd (1951).

‡Coughlin and O'Brien (1957).

TABLE 7. Coefficients of the C_P polynomials of Lrn (ambient P)[*]

T = 10-50 K	T = 50-293 K	T = 293-1000 K
k_0 = 8.0(2)E-1[†]	k_0 = -3.56(7)E1	k_0 = 2.121(1)E2
k_4 = -1.6(2)E-1	k_4 = 1.13(1)E0	k_1 = -9.69(5)E2
k_5 = 9.2(3)E-3	k_5 = -2.77(9)E-3	k_2 = -4.1(3)E6
	k_6 = 2.7(1)E-6	k_3 = 5.20(7)E8

[*] $C_P = k_0 + k_1 T^{-0.5} + k_2 T^{-2} + k_3 T^{-3} + k_4 T + k_5 T^2 + k_6 T^3$ (J mol^{-1} K^{-1}).

[†] E-n represents $\times 10^{-n}$.